Nitrogen fixation in mesoscale eddies of the North Pacific Subtropical Gyre: patterns and mechanisms

Mathilde Dugenne[a,b*†], Mary R. Gradoville[c*†],

Matthew J. Church[d], Benedetto Barone[a,b], Samuel T. Wilson[a,b], Uri Sheyn[a,b], Matthew J. Harke[e,f], Karin M. Björkman[a,b], Nicholas J. Hawco[a], Annette M. Hynes[g], François Ribalet[g], Angelicque E. White[a,b], David M. Karl[a,b], Edward F. Delong[a,b], Sonya T. Dyhrman[e,h], E. Virginia Armbrust[g], Seth John [i], John M. Eppley[a,b], Katie Harding[c], Brittany Stewart[c,i], Ana M. Cabello[c,j], Kendra A. Turk-Kubo[c], Mathieu Caffin[a,b], Jonathan P. Zehr[c]

[a] Department of Oceanography, University of Hawai‘i at Mānoa, Honolulu, HI, USA
[b] Daniel K. Inouye Center for Microbial Oceanography: Research and Education, University of Hawai‘i at Mānoa, Honolulu, HI, USA
[c] Ocean Sciences Department, University of California Santa Cruz, Santa Cruz, CA, USA
[d] Flathead Lake Biological Station, University of Montana, Missoula, MT, USA
[e] Lamont-Doherty Earth Observatory, Columbia University, Palisades, NY, USA
[f] Present Address: Gloucester Marine Genomics Institute, Gloucester, MA, USA
[g] School of Oceanography, University of Washington, Seattle, WA, USA
[h] Department of Earth and Environmental Sciences, Columbia University, New York, NY, USA
[i] Department of Earth Sciences, University of Southern California, Los Angeles, CA, USA
[j] Present address: Centro Oceanográfico de Málaga, Instituto Español de Oceanografía, Fuengirola, Málaga 29001, Spain

*Contributed equally

[†]Corresponding authors: dugennem@hawaii.edu, mgradovi@ucsc.edu

Running title: Nitrogen fixation in mesoscale eddies

Keywords: Cyanobacterial diazotrophs / nitrogen fixation / mesoscale eddies / physical accumulation / P-limitation / grazing rate estimates

Abstract

Recent studies suggest that mesoscale eddies may support elevated dinitrogen (N_2) fixation rates (NFRs) and abundances of N_2-fixing microorganisms (diazotrophs), yet the strength and mechanistic underpinnings of this trend are not fully understood. We explored the relationships among NFRs, cyanobacterial diazotroph abundances, and environmental conditions of mesoscale eddies by sampling three pairs of eddies of opposite polarity in the North Pacific Subtropical Gyre. Using the Hawaii Ocean Time-series for historical context, we found that NFRs were anomalously high (up to 18.6 nmol N L^{-1} d^{-1}) in the centers of two anticyclones. The highest NFR was linked to a positive anomaly in *Crocosphaera* abundance. To unravel the main processes and players, we used high-resolution abundance data, metatranscriptomes, deck-board incubations, and population models to evaluate three mechanisms for each diazotroph population: bottom-up control, top-down control, and physical control. Based on cell division and grazing rate estimates, *Crocosphaera* anomalies appeared to be partially driven by both bottom-up control (due to elevated surface phosphate concentration promoting high growth rates) and top-down control (reduced grazing pressure from putative predators). In contrast, although large, buoyant *Trichodesmium* and symbionts of diatoms (*Richelia*) appeared to have accumulated at the fronts between cyclonic and anticyclonic eddies, they had lower growth rates and contributed less to bulk NFRs. Together, the interplay of these three complex mechanisms may explain reports of elevated diazotroph abundances and NFRs associated with anticyclones and eddy fronts.

Introduction

In the oligotrophic North Pacific Subtropical Gyre (NPSG), the availability of nutrients limits photosynthesis in the sunlit layer, setting the upper bounds for marine trophic transfer and the amount of carbon (C) exported from the euphotic zone (Karl et al. 1996). Microorganisms with the ability to fix N_2 into bioavailable nitrogen (N), termed diazotrophs, thrive in the absence of dissolved inorganic nitrogen and introduce newly fixed N to otherwise N-limited phytoplankton (Karl et al. 2002). In the NPSG, most

N_2 fixation is achieved by diazotrophs smaller than 10 μm, mainly the unicellular cyanobacterial groups UCYN-A (symbionts of haptophytes), UCYN-B (*Crocosphaera*), and UCYN-C (*Cyanothece*-like organisms) (Zehr et al. 2001; Church et al. 2009). Other, larger cyanobacterial diazotrophs include filamentous *Trichodesmium* and Diatom-Diazotroph Associations (DDAs) with the symbiotic, heterocyst-forming *Richelia* and *Calothrix*. At Station ALOHA (A Long-term Oligotrophic Habitat Assessment, 22.75°N, 158.00°W), the field site of the Hawaii Ocean Time-series (HOT), N_2 fixation fuels up to half of new production and export from the euphotic zone (Karl et al. 1997; Böttjer et al. 2017). Monthly measurements show a high variability of bulk N_2 fixation rates (NFRs), which range from ~0.3-21 nmol N L^{-1} d^{-1} at the surface (Böttjer et al. 2017). Only a small portion of this variability is related to seasonality: NFRs generally peak during the late summer, when an annual pulse of particle export to the deep ocean has been putatively linked to blooms of DDAs (Karl et al. 2012; Poff et al. 2021). In addition to these large and recurrent blooms, fine-scale studies have highlighted the extreme patchiness of N_2 fixation in the NPSG, with diazotroph abundances and NFRs varying by orders of magnitude over relatively small temporal (<2 days) and spatial (<30 km) scales (Robidart et al. 2014; Gradoville et al. 2020).

The large variability in microbial community structure and NFRs at Station ALOHA (Karl and Church 2017) may be partially explained by the passage of mesoscale eddies, encompassing 31% of the observations over a 23-year period (Barone et al. 2019). Eddies entrap and perturb microbial seed populations due to the depression or uplift of nutrient-rich water layers in anticyclones and cyclones, respectively. For this reason, eddies have been linked to phytoplankton blooms and high rates of primary production (McGillicuddy and Robinson 1997). There is growing evidence that eddies also affect diazotrophic community structure and NFRs. Enhanced NFRs have been observed in anticyclonic eddies in many ocean regions, including the South Pacific Ocean, Indian Ocean, South China Sea, and Mediterranean Sea (Holl et al. 2007; Rahav et al. 2013; Löscher et al. 2016; Liu et al. 2020). At Station ALOHA, the highest NFRs have been observed under conditions of elevated sea surface height (characteristic of anticyclonic eddies) in summer months (Church et al. 2009; Böttjer et al. 2017).

Anticyclonic eddies in the NPSG have also been associated with the dominance of DDAs (Fong et al. 2008) and *Crocosphaera* (Wilson et al. 2017) during the summer. In addition, elevated *Trichodesmium* abundances have been observed in both cyclonic and anticyclonic eddies in the North Atlantic and North Pacific Oceans (Davis and McGillicuddy 2006; Taboada et al. 2010; Olson et al. 2015; Cheung et al. 2020).

There are several mechanisms through which eddies may influence N_2 fixation. N-depletion in the surface waters of anticyclones, driven by isopycnal downwelling, has been suggested to explain previous observations of high NFRs in anticyclonic eddies (Wilson et al. 2017; Liu et al. 2020). Eddies may also affect other bottom-up factors that control NFRs (i.e. phosphorus (P), iron (Fe), light, temperature) and work in concert with seasonal changes in temperature and diazotroph community structure (Church et al. 2009). The potential for eddies to affect top-down control has been less explored, but high grazing rates of diazotrophs and their hosts have been reported within mesoscale eddies (Landry et al. 2008; Wilson et al. 2017). Finally, vertical motions within eddies can lead to the physical accumulation of large diazotrophs such as *Trichodesmium* (Guidi et al. 2012; Olson et al. 2015). All of these mechanisms are modulated by specific life traits (e.g. buoyancy, size, symbiosis) and potential adaptations of individual taxa, suggesting that understanding diazotrophic diversity and activity within eddies is prerequisite to identifying the mechanisms driving variability in bulk NFRs.

We investigated the linkages among cyanobacterial diazotroph community structure, NFRs, and mesoscale eddies in the NPSG. N_2 fixation rates and diazotroph abundances were measured on three cruises which occupied pairs of cyclonic and anticyclonic eddies. We compare these data to the seasonal trends at Station ALOHA and use high-resolution diazotroph abundance data (via autonomous imaging flow cytometry), molecular approaches, and population models to explore the different mechanisms that may enhance NFRs and diazotroph abundances in mesoscale eddies.

Material and Methods

1. Eddy identification and characterization on three NPSG cruises

Between 2016 and 2018, three field expeditions sampled mesoscale eddies in the region north of the Hawaiian Islands. Observations took place between 9–14 May 2016 for the Hawai'i Ocean Experiment-Legacy 4 (KOK1606, *R/V Ka'imikai-O-Kanaloa*), 26 June–15 July 2017 for the Microbial Ecology of the Surface Ocean-Simons Collaboration on Ocean Processes and Ecology (KM1709, *R/V Kilo Moana*), and 27 March–10 April 2018 for the Hawaiian Eddy Experiment (FK180310, *R/V Falkor*).

Prior to each cruise, cyclonic and anticyclonic eddies were identified via satellite-derived sea level anomalies (SLA, Fig. 1). Additionally, Finite Size Lyapunov Exponents (FSLE), measuring the divergence rate of parcels of water close in space, were extracted along the cruise track from the daily satellite product distributed by Copernicus (marine.copernicus.eu/) and AVISO (www.aviso.altimetry.fr/), respectively.

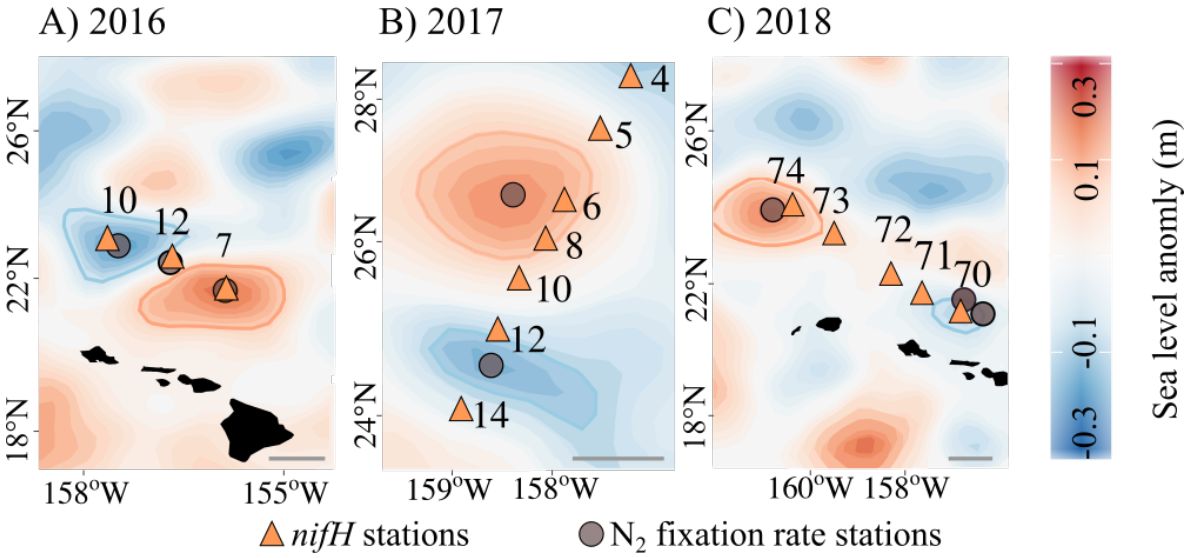

Figure 1: Sampling locations for *nifH* gene abundances (triangles) and N_2 fixation rates (circles) across each pair of eddies during the 2016 (A), 2017 (B), and 2018 (C) cruises. Sampled cyclones are indicated by negative sea level anomalies (-0.1 m blue contour) and sampled anticyclones by positive sea level anomalies (0.1 m red contour). Scale bars: 100 km.

Daily SLA was corrected for the interannual trend and seasonal cycle following Barone et al. (2019). In the Northern hemisphere, cyclonic eddies are characterized by a depression of the sea surface height (negative

SLA) enclosed by anticlockwise circulation while anticyclones present elevated sea surface height (positive SLA) and clockwise circulation. Eddies were tracked in time using daily maps of corrected SLA centered in a 1.5° window around the locations of the eddy centers in order to extract their age and the amplitude of SLA during the sampling periods. In addition, the phase of each eddy was determined using the variability of SLA (ΔSLA) within 10 d before and after the sampling periods, calculated as the slope of the linear regression of ΔSLA over time (Table 1).

Table 1. Characteristics of eddies sampled during the three cruises. ΔSLA/Δt was calculated using the variability of SLA within 10 d before and after the sampling periods.

		Anticyclones				Cyclones			
Year	Season	Phase	Age (d)	Amplitude (m)	ΔSLA/Δt (cm d^{-1})	Phase	Age (d)	Amplitude (m)	ΔSLA/Δt (cm d^{-1})
2016	Spring	intensifying	88	0.25	0.32	stable	112	-0.19	0.01†
2017	Summer	stable	83	0.26	0.04†	weakening	246	-0.14	0.11
2018	Spring	stable	95	0.21	0.02†	weakening	212	-0.14	0.26

†: Not significant

All three cruises included a mapping phase, in which samples were collected along a transect spanning one eddy to the other in order to characterize the water column, quantify diazotrophs via *nifH* gene abundances and cell counts, and measure NFRs. The 2017 and 2018 cruises also included Lagrangian surveys along Surface Velocity Program drifter trajectories in one or both eddy centers, with continuous imaging of near surface plankton communities to assess high resolution temporal dynamics.

Downwelling cosine photosynthetically active radiation (PAR) was measured using a LI-190 (LI-COR Environmental, Lincoln, NE, USA) on the ship's deck, propagated with depth using the fraction of incident PAR (%) measured at 1 m-intervals from a free-falling optical profiler (Satlantic HyperPro, Sea-Bird Scientific, Bellevue, WA, USA) and corrected (× 1.2) to convert downwelling irradiance into a scalar irradiance (Wozniak et al. 2003; Letelier et al. 2017). In the text hereafter, we refer to the scalar irradiance as PAR. A Conductivity-Temperature-Depth (CTD) rosette was used to collect depth profiles of

temperature, salinity, and potential density anomalies, as well as samples for dissolved inorganic phosphate (PO_4^{3-}) and dissolved inorganic nitrogen (NO_3^-+NO_2^-). PO_4^{3-} concentrations were measured using the approach described by Karl and Tien (1992) with a precision of ± 1 nmol L^{-1} and detection limit of 3 nmol L^{-1}. NO_3^-+NO_2^- concentrations were measured by chemiluminescence with a detection limit of 1 nmol L^{-1}, as described in Foreman et al. (2016). Dissolved Fe (dFe) for the 2017 cruise was collected using a trace metal clean sampling rosette with external spring Niskin® bottles. For the 2018 cruise, samples for dFe were collected in Go-Flo® bottles mounted on a non-metallic line and triggered with a PTFE messenger. Iron concentrations were determined by inductively coupled plasma mass spectrometry using isotope dilution (Pinedo-González et al. 2020). Particulate Fe concentrations from the 2017 cruise (Table S1) were filtered onto a 0.2 μm Supor® membrane (MilliporeSigma, Burlington, MA, USA) and digested at high temperature in 50% nitric acid, as described by Hawco et al. (2020a).

2. Biogeochemical rates

2.1 N_2 fixation rates

NFRs were measured on all cruises using the $^{15}N_2$ uptake method of Montoya et al. (1996), with modifications to avoid incomplete dissolution of $^{15}N_2$ gas (Mohr et al. 2010; Wilson et al. 2012). During the 2017 and 2018 cruises, NFRs were measured using in situ arrays in eddy centers. Seawater was collected pre-dawn from 5, 25, 45, 75, 100, and 125 m using Niskin® sampling bottles attached to the rosette. Collected seawater was subsampled into triplicate 4.4 L acid-washed, milliQ-rinsed polycarbonate bottles which were spiked with $^{15}N_2$ tracer (see below), attached to the free-floating arrays, and incubated for 24 h at the depth from which they had been collected.

During the 2016 cruise, surface NFRs were measured in the center of each eddy and at an additional station between eddies (Station 12, Fig. 1). Seawater was collected from 25 m and sampled into 4.4 L bottles (as described above), spiked with $^{15}N_2$ tracer, and incubated in surface-seawater cooled, flow-through, deck-board incubators fitted with screening to reproduce in situ light conditions. These incubations were conducted during the day (10 h incubation, 08:00-18:00 local time) and at night (6 h

incubation, 22:00-04:00 local time), using seawater from separate CTD casts prior to each incubation. Hourly daytime and nighttime rates (Fig. S1) were multiplied by the total hours of daylight and darkness (~13 and 11 h, respectively) and summed in order to calculate daily NFRs.

For all cruises, the $^{15}N_2$ tracer was added as $^{15}N_2$-enriched seawater. Prior to each cruise, surface seawater was collected from Station ALOHA, filtered through a 0.2 μm in-line filter, and transported in the dark to the University of Hawai‘i, Mānoa. There, the seawater was degassed, injected with ~13 mL $^{15}N_2$ gas (99 atom %, Cambridge Scientific, Watertown, MA, USA) per L seawater, and manually agitated to dissolve the gas bubble, as described by Wilson et al. (2012). This $^{15}N_2$-enriched seawater was dispensed into glass serum bottles which were crimp-sealed, stored at 4°C, and brought to sea. To initiate incubations, 100 mL of seawater was withdrawn from each full 4.4 L incubation bottle and replaced with 100 mL of $^{15}N_2$-enriched seawater. The $^{15}N/^{14}N$ ratio of each batch of $^{15}N_2$-enriched seawater was measured using membrane inlet mass spectrometry according to Ferrón et al. (2016). These values were used to calculate the initial atom % of $^{15}N_2$ for each incubation. A recent study by White et al. (2020) indicates that measuring the $^{15}N_2$ atom % of the enriched seawater rather than the final inoculum may lead to underestimation of the initial $^{15}N_2$ atom % values. For the eddy and HOT observations, this could result in a relatively small (<20%) overestimation of rates.

All $^{15}N_2$ incubations were terminated by filtering (via a peristaltic pump or vacuum filtration) onto pre-combusted (5 h at 450°C) 25 mm glass fiber filters (GF/F, Whatman, Maidstone, UK). Additional 4.4 L seawater samples were collected from each sampling depth for $\delta^{15}N$ natural abundance measurements; these samples were immediately filtered at the start of each incubation. All filters were frozen at -20°C or -80°C and transported to the University of Hawai‘i, Manoa, where they were dried at 60°C overnight and packaged into tin capsules (Costech Analytical Tech Inc, Valencia, CA, USA). Concentrations and isotopic composition ($\delta^{15}N$) of particulate N were analyzed via continuous-flow isotope ratio mass spectrometry using a Carlo-Erba EA NC2500 coupled with Thermo Finnigan DeltaPlus XP at the University of Hawai‘i

Biogeochemical Stable Isotope Facility. NFRs and detection limits were calculated according to Montoya et al. (1996) (Table S2).

Historical NFRs at Station ALOHA (measured from 2012-2019 as part of the HOT and Simons Collaboration for Ocean Processes and Ecology programs) are presented to provide seasonal and interannual context for the three individual expeditions that occurred in 2016, 2017, and 2018. The time-series dataset from 2012-2014 was previously published by Böttjer et al. (2017) and is extended to 2019 in this publication with no alteration to methodology or data processing procedures. As described in Böttjer et al. (2017), measurements were conducted using the $^{15}N_2$-enriched seawater method (see above).

2.2 P-uptake rates

Size-fractionated (>2 μm) PO_4^{3-}-uptake rates were quantified over the Lagrangian surveys conducted during the 2017 cruise, following the protocol of Björkman et al. (2012). Briefly, seawater was collected pre-dawn from 15 m, sampled into duplicate 75 mL polycarbonate bottles, spiked with a radiotracer in the form of ^{33}P-orthophosphate (PerkinElmer NEZ008, carrier free, Waltham, MA, USA), and incubated in on-deck incubators, as described above, for 6-8 h. After incubation, 10 mL subsamples were filtered onto 2 μm Millipore GTTP polycarbonate membrane filters (MilliporeSigma). Filters were rinsed 3 times with 5 mL of filtered seawater and placed into scintillation vials. Scintillation cocktail (Ultima Gold LLT, PerkinElmer) was added to each vial and the radioactivity was counted with a PerkinElmer liquid scintillation counter (PerkinElmer TriCarb 2910). Uptake rates (nmol P L^{-1} d^{-1}) were calculated from the ^{33}P activity retained on the filters, the measured ^{33}P addition, and the phosphate concentration of the samples.

3. Diazotroph abundances

3.1 DNA extraction and *nifH* gene quantification

The *nifH* genes of eight major cyanobacterial diazotroph groups were quantified using digital droplet polymerase chain reaction (ddPCR) (Fig. S2). During the 2016 and 2018 cruises, seawater for ddPCR was collected from depth profiles at the same stations sampled for $^{15}N_2$ incubations. During the

187 2017 cruise, seawater for ddPCR was collected from depth profiles within each eddy, but from separate
188 stations than those used for the $^{15}N_2$ arrays (Fig. 1). For all cruises, seawater was collected using sampling
189 bottles attached to the CTD rosette and subsampled into duplicate (2018) or single (2016 and 2017) 4.4 L
190 acid-washed, milliQ-rinsed polycarbonate bottles. A peristaltic pump was used to filter 4 L of seawater
191 onto 0.2 µm pore-size Supor® membranes (Pall Corporation, Port Washington, NY, USA), which were
192 placed into microcentrifuge tubes containing mixtures of 0.1- and 0.5-mm glass beads (Biospec Products,
193 Bartlesville, OK, USA), flash-frozen in liquid N_2, and transported to the University of California, Santa
194 Cruz, where they were stored at -80°C until analysis.

195 DNA was extracted using the DNeasy Plant Mini Kit and the QIAcube instrument (Qiagen, Venlo,
196 Netherlands). Extractions followed the manufacturer's protocol with additional steps of three flash
197 freeze/thaw cycles, bead-beating for two min, and a Proteinase K treatment, as described by Moisander et
198 al. (2008). The final DNA elution volume was 100 μL. DNA extracts were stored at -20°C prior to ddPCR.

199 Duplicate ddPCR reactions were performed for each sample using the ddPCR Supermix for Probes
200 (no dUTP) (Bio-Rad Laboratories, Hercules, CA, USA) with probes using either 6-FAM™ or HEX™
201 chemistry (Integrated DNA Technologies, Coralville, IA, USA). References for all primers and probes are
202 provided in Table 2. Note that the assay targeting UCYN-A3 (quantified during the 2016 and 2018 cruises
203 only) also targets UCYN-A2; however, *nifH* sequencing data suggest that UCYN-A2 is rare at Station
204 ALOHA (Cornejo-Castillo et al. 2019). Final reactions (after droplet generation) were 20 μL and consisted
205 of 1X Supermix, 0.4 μmol L^{-1} forward primer, 0.4 μmol L^{-1} reverse primer, 0.2 μmol L^{-1} probe, and 1.6
206 μL DNA. Droplets were generated using a Bio-Rad Automated Droplet Generator and cycled on a Bio-Rad
207 1000 Touch™ Thermal Cycler. Thermocycling reactions were as follows: 95°C for 10 min, followed by 40
208 cycles of 94°C for 30 s then 64°C for 1 min, and finally 98°C for 10 min, except for the UCYN-B, UCYN-
209 C, and *Trichodesmium* assays, which used an annealing temperature of 60°C rather than 64°C. The optimal
210 annealing temperature for each assay was empirically tested prior to running samples. *Trichodesmium*

211 (FAM) and UCYN-C (HEX) assays were run simultaneously in the same wells; multiplex tests prior to

212 running samples indicated no cross-reactivity between *Trichodesmium* and UCYN-C primers or probes.

213 **Table 2.** Characteristics of the main groups of cyanobacterial diazotrophs found in the NPSG.

Diazotroph taxa		Biomass			Stoichiometry			Fixation Time[a]	Refs
nifH genus	Known symbiont *: obligate	Size μm	*nifH* observed genes cell^{-1}	C quota fg C μm^{-3}	C:P mol:mol	C:N mol:mol	C:Fe mol:μmol	Day (D)/ Night (N)	*nifH* primer/ probe set
UCYN-A *Atelocyano-bacterium*	*Braarudo-sphaera**	1-3.3[n]	0.49-27.8[m]	480[b]				D	Church et al. (2005a); Thompson et al. (2014)
UCYN-B *Crocosphaera*	*Climacodium*	1.5-3[c] 4-8[p]	3.6[c]	456 ± 76[b]	150[j]	6.1[r]	0.06 ± 0.11[h]	N	Moisander et al. (2010)
UCYN-C *Cyanothece*-like		4-6[d]	1.1[p]	233 ± 88[l]	135 ± 16[i]	6.14[i]	13 ± 3[g]	N	Foster et al. (2007)
Het1 *Richelia*	*Rhizosolenia*	2-14[e]	6.7-2007.8[f]	168 ± 83[l]	141.5 ± 10.8[k]	7.3[k]		D	Church et al. (2005b)
Het2 *Richelia*	*Hemiaulus*	2-8[e]	6.7-2007.8[f]	168 ± 83[l]	141.5 ± 10.8[k]	7.3[k]		D	Foster et al. (2007)
Het3 *Calothrix*	*Chaetoceros*	3-6[e]	6.7-2007.8[f]	195 ± 88[l]	141.5 ± 10.8[k]	7.3[k]		D	Foster et al. (2007)
Tricho *Trichodesmium*		6.5-7[b]	2.6-1012.5[f]	181 ± 4[b]	62[g]	5.5[o]	0.03 ± 0.01[q]	D	Church et al. (2005a)

[a]: Zehr (2011) [b]:Goebel et al. (2008) [c]: Wilson et al. (2017) [d]: Taniuchi et al. (2012) [e]: Tuo et al. (2017) overall range for the heterocyst and vegetative cells [f]: White et al. (2018) heterocyst-based estimates for DDAs [g]: Berman-Frank et al. (2007) under low Fe concentration [h]: Tuit et al. (2004) in Fe-depleted cultures [i]:Finkel et al. (2006) under low irradiance [j]: Garcia et al. (2015) [k]:Follett et al. (2018b), minimum stoichiometry derived from bulk filters collected during a DDA bloom [l]: Estimated using equation the Verity et al. (1992) relating nano-phytoplankton biovolume to carbon content [m]: Krupke et al. (2013) [n]: Cornejo-Castillo et al. (2019) [o]: White et al. (2006) [p]: This study [q]: Berman-Frank et al. (2001) in Fe-depleted cultures [r]: Knapp et al. (2012) under low NO_3^- concentration

214 The fluorescent signals of amplified droplets were measured using a Bio-Rad QX200 Droplet

215 Reader and data were analyzed using the QuantaSoft™ Analysis Pro software. Manual thresholding was

216 used to differentiate positive from negative droplets, and samples with <10,000 total droplets were

217 discarded. Positive control reactions and no template control reactions were included on all runs. Detection

218 limits were calculated as 3 times the standard deviation of no template control reactions and were

219 evaluated separately for each assay (Fig. S2).

220 The historical HOT *nifH* gene abundances of UCYN-A1, UCYN-B, *Trichodesmium*, Het-1, Het-2,

221 and Het-3, measured from 2004-2017 using quantitative PCR (qPCR), are provided for seasonal context

222 (Church et al. 2009, dataset doi: 10.5281/zenodo.4477269). Details on sample collection, DNA extraction,

223 and qPCR are provided in Church et al. (2009). All qPCR assays except for Het-2 and Het-3 used the same
224 primer/probe sets as the corresponding ddPCR assays for the eddy cruises. Het-2 was quantified using the
225 primer/probes sets of Church et al. (2008) and Het-3 used the same forward and reverse primers as Foster
226 et al. (2007) but the probe sequence contained an extra adenine on the 3' end.

227 **3.2 Enumeration by autonomous flow cytometry**

228 The size and concentrations of large (>4 μm) free-living and filamentous diazotrophs, including
229 *Trichodesmium* (single filaments), *Richelia* (free and symbiotic heterocyst-containing filaments), *Calothrix*
230 (unattached and epiphytic heterocyst-containing filaments), and large-size *Crocosphaera* (free-living),
231 were estimated by automated imaging flow cytometry (Imaging FlowCytobot [IFCb], McLane, East
232 Falmouth, MA, USA) during the 2017 and 2018 cruises. The IFCb detects individual particles via laser-
233 induced fluorescence and light scattering used to trigger image acquisition of all particles in successive ~5
234 mL samples (analyzed in ~20 min). The detection limit therefore approximates 200 cells L^{-1}, equivalent to
235 one detected cell per 5 mL sample. Each 20-min interval analysis was sampled from the ship's
236 uncontaminated underway system, which continuously pumped seawater from ~7 m depth. During the
237 analysis, individual images of single or colonial cells were collected along with their optical fingerprints
238 (light scattering and chlorophyll fluorescence).

239 A training set of images was used to classify organisms to the genera level based on morphological
240 traits, as described in Dugenne et al. (2020). The output of the random forest classifier (Sosik and Olson
241 2007) was corrected by manually annotating misclassified images to provide accurate estimates of the cell
242 size distribution and concentration of individual genera. We evaluated the biomass of diazotrophs over
243 time using the cell or filament concentration multiplied by their average biovolume-to-C quota (Menden-
244 Deuer and Lessard 2000) in 2017 (Fig. S3) and 2018 (Fig. S4). Standard errors associated with the
245 intercept (±0.08 $\log_{10}$pg C) and slope (±0.02 $\log_{10}$pg C μm^{-3}) of the biovolume-to-C regression result in a
246 ±20% uncertainty of diazotroph biomass. Importantly, *Trichodesmium* biomass is underestimated as the
247 fixed camera field of the IFCb prevents the visualization of both apical cells when the colony size exceeds

425 μm, the operational size of the camera field. The histogram of *Trichodesmium* filament length measured by the IFCb for the 2017 and 2018 cruises was compared to microscopic slides from 5 and 15 m prepared during the 2017 cruise (Fig. S5) following the protocol of White et al. (2018). According to the size distribution of filaments counted by microscopy (n=636), the IFCb-derived biomass was underestimated by 23 ± 5% (n=3); we therefore corrected biomass observations to match the microscopy by multiplying estimates by 1.23.

Small-size *Crocosphaera* (2-4 μm, Fig. S3) were enumerated using an autonomous SeaFlow flow cytometer (Ribalet et al. 2019). Briefly, the SeaFlow was used to continuously sample surface seawater from the ship's uncontaminated underway system, acquiring optical measurements of light scatter, red fluorescence, and orange fluorescence (characteristic of the phycoerythrin-containing *Crocosphaera*) at 3 min intervals. The population of small-size *Crocosphaera* was gated over time to estimate abundance and the average light scatter-to-size ratio derived from Mie theory (Ribalet et al. 2019). The average equivalent spherical diameter was converted to biovolume and C to determine the biomass of the population every hour.

3.3 Comparison of *nifH* gene abundance to cell counts and patchiness correction

We compared the surface (5 m) *nifH* gene abundances measured during the 2017 and 2018 cruises to the underway (7 m) cell concentrations of diazotrophs detected by autonomous flow cytometry within 2 h of the DNA sample collection (Fig. S5). Since large diazotrophs (*Trichodesmium, Richelia,* and *Calothrix*) tend to have patchy distributions and often had low *nifH* gene abundances that were close to the IFCb detection limit, we aggregated 4 consecutive samples (1.5-2 h measurement window and ~20 mL volume) from the IFCb to improve the comparison between cell and *nifH* gene abundances.

4. Diazotroph populations models

Several modelling approaches were used to explore how eddies affect N_2 fixation by modulating diazotroph growth and loss rates (Table S3). During vegetative growth, diazotrophs divide by binary fission. Binary fission is generally described as the separation of a mother cell into 2 daughter cells after

completion of the cell cycle, except for DDAs which follow an alternate mode of division whereby the entire filament divides near its center (Villareal 1989). In the absence of losses, these divisions result in an increase of population abundances at a rate μ, defined here as the intrinsic growth rate. We assumed that the growth of photosynthetic diazotrophs was mainly affected by abiotic factors (nutrient concentrations, light, and temperature) whose effects have been characterized in culture-based studies. Using parameters from these studies, we provide a broad overview of the effect of eddies on diazotroph cell division by modeling how intrinsic growth rates varied as a function of the environmental gradients observed across each pair of eddies (Section 4.1), except for the 2016 cruise when iron concentrations were not measured. Additionally, we obtained independent estimates of growth rates by tracking dividing cells or filaments within each diazotroph population using continuous imaging during the intensive Lagrangian surveys conducted at the surface of each eddy center (Section 4.2). In this framework, the dynamics of diazotroph populations depend on the net balance between bottom-up and top-down processes. Top-down processes were partially explored using the co-occurrence of various predators imaged by the IFCb to model predator-prey interactions and estimate grazing rates upon diazotrophs in each eddy (Section 4.3). Other processes can influence the loss of diazotrophs, including viral lysis, programmed cell death, vertical migration, entrainment of water at the base of the mixed layer, and sinking; these processes were not assessed in the present study. Despite the different assumptions and uncertainties of our three models, the integration of rate estimates provides a unique opportunity to evaluate diazotroph production (e.g. C, N, P) and determine which taxa contributed to elevated NFRs in anticyclones (Section 4.4).

4.1 Prediction of diazotroph growth rates across transect

We compiled growth rates from laboratory cultures of diazotrophs grown under diverse limiting factors in order to model the effects of observed temperature, light, and inorganic nutrient concentrations on diazotroph division using environmental parameters reported in Table 3. Cross-sections of temperature (T), daily average instantaneous PAR (E), PO_4^{3-}, and dFe concentrations from depth profiles during the 2017 and 2018 cruises were used to predict diazotroph growth rates and growth-limiting factors according

to Liebig's law of the minimum (Eq. 1). Unlike common models that use variable maximum growth rates as a function of temperature or light, we have integrated the effects of all abiotic factors on population theoretical maximum rate (μ_{max}) measured in replete cultures to include light and temperature as potential limitations. Surface predictions were also compared to observed surface growth rates across eddies measured during Lagrangian surveys (see Section 4.2) using a Student statistical test (Table S3). Since environmental parameters may vary greatly depending on the model formulation (see Tian 2006 for a review of the common formulations used to model phytoplankton growth), we consistently fitted the same formulation to each diazotrophic population using the nonlinear least-squares R function 'nls'.

(1) $\mu(T,E, PO_4^{3-},dFe) = \mu_{max} \times \min(f_\mu(T),f_\mu(E),f_\mu(PO_4^{3-}),f_\mu(dFe))$

where f_μ designate unitless limiting functions, representing the changes of diazotroph growth rates relative to their maximum.

The change of growth rates over a 10°C temperature increase (Q_{10}, reported in Table 3) is used to express the temperature-dependence of population relative growth rates when temperatures are below their thermal optimum (T_{opt}, °C), similar to the Arrhenius function for enzyme activities:

(2) $f_\mu(T) = Q_{10}^{\frac{T-T_{opt}}{10}}$

with T_{opt} the optimal temperature for which f_μ (T_{opt})=1. Note that in our study temperatures never reached the thermal optimum for any diazotroph taxa examined (Table 3), but alternative models should be used in order to express the deleterious effect of temperatures above the thermal optimum. To our knowledge, the thermal adaptations of *Richelia* and *Calothrix* have not been characterized in cultures. When parameters were not available, we excluded the corresponding formulation from Eq. 1 (f_μ (T) in the case of DDAs). Similar ecological models predicting the growth of DDAs in the Atlantic (Stukel et al. 2014) and the NPSG (Follett et al. 2018a) have excluded the effect of temperature.

322 **Table 3.** Environmental parameters influencing growth rates of cyanobacterial diazotrophs in cultures. All

323 parameters are based on changes in growth rates unless otherwise noted (marked by **).

Genus strain	Temperature		Light		Nutrient limitation	
	μ_{max} (d^{-1})	Q_{10} (T_{opt}) unitless	E_k (μmol quanta m^{-2} s^{-1})	E_c (μmol quanta m^{-2} s^{-1})	$k_{PO_4^{3-}}$ (nmol L^{-1})	k_{Fe} (nmol L^{-1})
Crocosphaera WH0401 (small)	0.58[m]	1.57 ± 0.19[c] (30 °C)	84 ± 2.2[m]	19 ± 7[m]		
WH0003 (large)	0.86[d]	1.33 ± 0.28[c] (30 °C)	78 ± 4.4[d]	22 ± 4[d]	75 ± 12.4[i]	0.35[j] (WH8501)
Cyanothece BG043511 (coastal)	0.8[a]	3.08 ± 0.39[a] (34°C)				
TW3 (open ocean)	0.71 [b]	1.03 ± 0.68 [b] (30°C)	78 ± 1.4[b]	20 ± 8[b]		
Richelia	0.60[f]		30 ± 1.7[f]	9 ± 2[f]	130[l]	0.5[l]
Calothrix	0.51[g]		232 ± 5[h]	-182 ± 42[h**]	130[l]	0.5[l]
Trichodesmium IMS101	0.33[e]	2.31 ± 0.07[n] (28°C)	149 ± 33[e]	14 ± 9[e]	50 ± 24[i]	0.14[k]

[a]: Brauer et al. (2013) [b]: Taniuchi et al. (2012) [c]: Fu et al. (2014) [d]:Garcia et al. (2013b) [e]: Boatman et al. (2017) [f]: Villareal (1990) Note that μ_{max} (d^{-1}) was derived from division rates of 0.87 div d^{-1}x $\log_e(2)$ [g]: This study [h**]: Foster et al. (2010) Note that parameters are based on N_2 fixation rates not growth rates [i]: Garcia et al. (2015) for cultures maintained at low dFe concentration (0.12-0.35 nM) [j]: Jacq et al. (2014) for a strain of ~3.5 μm according to Webb et al. (2009) [k]: Boatman et al. (2018) [l]: Follett et al. (2018a) [m]: Garcia et al. (2013a) [n]: Breitbarth et al. (2007). Definition of the parameters: μ_{max} (theoretical maximum growth rate, Eq. 1), Q_{10} (Arrhenius coefficient, Eq. 2), T_{opt} (optimal temperature, Eq. 2), E_k (light saturation coefficient, Eq. 4), E_c (light compensation coefficient, Eq. 3), $k_{PO_4^{3-}}$ / k_{Fe} (half-saturation coefficients, Eq. 5). Note that k_{Fe} is based on culture kinetics of dissolved inorganic iron (Fe') uptake for *Crocosphaera* and *Trichodesmium*, which is assumed to be the only form of iron bioavailable, and from allometric scaling for DDAs.

324

325 We used a modification of the hyperbolic tangent function described in Jassby and Platt (1976) to

326 express the change in relative growth rates as a function of the average instantaneous light intensity, E

327 (μmol quanta m^{-2} s^{-1}), and the compensation light intensity E_c (μmol quanta m^{-2} s^{-1}):

328 (3) $f_\mu(E) = tanh\left(\frac{\alpha(E - E_c)}{\mu_{max}}\right)$

329 Note that we introduced E_c to accommodate the growth of *Trichodesmium* (Boatman et al. 2017) and

330 *Crocosphaera* (Garcia et al. 2013b). The light saturation parameter, E_k (μmol quanta m^{-2} s^{-1}), is then

331 defined using the maximum growth rate, μ_{max}, reported in Table 3 and the initial slope of μ-E curve, α, as:

332 (4) $E_k = \frac{\mu_{max}}{\alpha} + E_c$

Finally, we used the Michaelis-Menten formulation for enzyme kinetics to express the change of relative growth rate as a function of PO_4^{3-} or dFe concentration (nmol L^{-1}):

$$(5)\ f_\mu(PO_4^{3-}) = \frac{PO_4^{3-}}{PO_4^{3-} + k_{PO_4^{3-}}}, \qquad f_\mu(dFe) = \frac{dFe}{dFe + k_{Fe}}$$

4.2 Estimation of diazotroph in situ growth rates in eddy centers

We estimated diazotroph growth rates, μ(FDC)(d^{-1}), near the surface from the presence of dividing *Crocosphaera, Richelia, Calothrix,* and *Trichodesmium* imaged with the IFCb (Table S3). The fraction of dividing cells noted FDC, marking the stage prior to cell division, was detected over time within the Lagrangian sampling periods of the 2017 and 2018 cruises in order to calculate daily growth rates following the formulations of McDuff and Chisholm (1982):

$$(6a)\ \mu(\mathrm{FDC}) = \log_e\left(\frac{[1+\max(\mathrm{FDC})]}{[1+\min(\mathrm{FDC})]}\right) \text{ for DDAs}$$

$$(6b)\ \mu(\mathrm{FDC}) = \frac{1}{n(t_d)}\sum_{i=1}^{n}\log_e(1+\mathrm{FDC}_i) \text{ for } \textit{Crocosphaera} \text{ and } \textit{Trichodesmium}$$

where n is the number of samples in a 24 h cycle, t_d (d) is the duration of the terminal event marking the effective separation of dividing cells (cytokinesis), and FDC is the fraction of dividing cells/filaments. Eq. 6a was used for DDAs as this approach, commonly reffered as the f_{max} approach, does not require prior knowledge on t_d. Conversely, we used Eq. 6b for *Crocosphaera* and *Trichodesmium* since estimates for the duration of cell division were available in cultures (see Supplementary text S1). As reviewed in McDuff and Chisholm (1982), this estimate represents a better approximation of true intrinsic growth rates when populations are fast-growing (μ >0.69 d^{-1}) or not phased to a single light-dark cycle. Estimates of μ(FDC) for each Lagrangian sampling period are reported in Table S3 and described in Supplementary Text S1 with their uncertainties.

As a result of low concentrations and patchy distributions of diazotrophs, all in situ growth rates were estimated by aggregating samples in a 6 h window in order to observe enough filaments of *Trichodesmium*, *Richelia*, and *Calothrix.* The number of observations for each population, the fractions of dividing diazotroph cells or filaments, daily growth rate estimates, and growth rate uncertainties are

reported in Table S4. We discarded days with standard error >30% (due to the low number of observations) before calculating the average and standard deviation of diazotroph growth rates in each eddy (Table S3). The 6 h sample aggregation caused an underestimation of μ(FDC), as described McDuff and Chisholm (1982); thus, we consider that the growth rates reported in Table S3 and the results section constitute a lower-bound of the true population growth rates.

A series of enrichment incubations were conducted during the 2017 Lagrangian surveys to test whether diazotrophs were nutrient-limited. Ten L carboys were filled with seawater collected from the standard (i.e. not trace-metal free) CTD-rosette from 15 m and incubated for four days in deck-board incubators described above, either with (+NPFe) or without (Control) NO_3^-, PO_4^{3-}, and dFe at respective final concentrations of 6 μmol L^{-1}, 0.5 μmol L^{-1}, and 5 nmol L^{-1}. Note that due to the mode of sample collection, both the control and replete treatments likely contained dFe concentrations above background levels. Also, it is possible that NO_3^- additions within these incubations may have influenced diazotroph growth rates and/or NFRs; the extent to which fixed N inhibits NFRs is not well-understood (Knapp 2012). Fifteen mL triplicates were analyzed by the IFCb at T_0 and T_{final} (T_0 + 4 days) and the log-difference of the endpoint abundances were used to estimate and compare the net growth rates of several diazotrophs under control and replete conditions (Fig. S6). Populations of *Richelia* and *Calothrix* were too sparse to estimate growth rates in the control treatment.

We tested the differences in in situ growth rates between eddy types and between treatments in deck-board incubations by generalized linear regression, assuming a quasi-Binomial distribution to address data over-dispersion, weighted by the uncertainties of the daily estimates with the R function glm(μ~Eddy/Treatment, family=quasibinomial(link = 'logit'),weights=1/ σ^2(μ(FDC))).

4.3 Estimation of diazotroph mortality using a predator-prey model

We used a Generalized Lotka-Volterra model to describe the temporal changes in the abundance of diazotrophs (x_i, cells L^{-1}) as a function of their growth rate (r_i, d^{-1}) and specific interactions (a_{ij}) with other

populations (x_j, cells L^{-1}) imaged by the IFCb throughout eddy Lagrangian surveys (2017 and 2018 cruises):

$$(7)\ \frac{dx_i}{dt} = x_i(r_i + \sum_j a_{ij}x_j)$$

with r depending on μ, the intrinsic growth rate, and l a linear loss rate due to processes that are not explicitly accounted with the biological interactions tested (e.g. viral lysis, programmed cell death, additional grazing from populations not imaged by the IFCb, vertical migration, mixed layer entrainment, and/or sinking). The strength of the interaction between populations *i* and *j* is determined by the coefficient a_{ij} and population abundances and can be interpreted as different biological rates depending on the type of the interaction. When coefficients a_{ij} and a_{ji} are negative and positive respectively, *j* grows at *i*'s expense, as would a putative grazer of the diazotroph *i*. Conversely, two negative coefficients indicate resource competition between populations. When possible, we looked for visual evidence of diazotrophic prey ingestion using the IFCb images from 2017 and 2018 to confirm the interaction between diazotrophs and their putative grazers.

In order to identify grazing interactions between diazotrophs and other protists in each eddy center, all pairs of interaction coefficients were estimated by a linear multi-regression model fitted to the changes in population abundances throughout the Lagrangian sampling within individual eddies as follows:

$$(8)\ \frac{\Delta \ln(x_i)}{\Delta t} = y = r_i + \sum_j a_{ij}x_j$$

with Δt, a 30 min interval, r_i, the intercept of the linear regression, and a_{ij}, the linear coefficient for the interaction with population *j*.

Since the regression included a large number of coefficients, accommodating 103 different populations in 2017 and 89 populations in 2018, we used a regularized Lasso regression implemented in the 'glmnet' R package to penalize non-significant interactions (Tibshirani et al. 2012). To test whether the remaining interaction coefficients between diazotrophs and their putative predators were significant, we used the Student statistics, knowing the standard error of the linear regression estimate se(a_{ij}):

(9) $t = \frac{a_{ij}-0}{se(a_{ij})} \sim$ Student's t distribution

where se(a_{ij}) scales to the coefficient a_{ij} (slope=0.1017, p-value<0.001, R^2=0.99, n=5), resulting in a 10% uncertainty in the grazing rate estimates (Dugenne et al. 2020). Significant coefficients were sorted to determine the importance of protists grazing pressure g_j (d^{-1}), defined as the product of coefficient a_{ii} and the abundance of grazer population j. Predator in situ growth rates, estimated from the detection of doublet cells reported in Table S4, are provided in Fig. S7 and were compared to the estimates of grazing rates when possible. We used a hierarchical cluster analysis (R function 'hclust') to group individual grazing rates g_j together based on their Euclidian dissimilarities (R function 'dist'). In the absence of dilution experiments during the eddy cruises, we estimated the grazing rate of diazotrophs, g (d^{-1}), by summing all the predator grazing rates predicted by the Generalized Lotka-Volterra model (Eq. 10):

(10) $g = \sum_j g_j = \sum_j a_{ij} x_j$ with a_{ij} negative and a_{ji} positive.

The overall grazing rate g upon each diazotroph is reported in Table S3. Since we only accounted for interactions between populations that were quantified by the IFCb, these estimates should provide a minimum estimate for specific grazing rates since rare (<200 cells L^{-1}) protists were not included. Predation by protists smaller than 4 μm could not be assessed due to size limitations of the IFCb; however, grazing upon diazotrophs by this size class is unlikely as most planktonic grazers ingest prey smaller than their own size (Hansen et al. 1994). Additional losses, including predation by rare grazers or viruses, are accounted for in the term r, also estimated in the model. The ratio of overall grazing relative to prey growth (g:μ), with μ, the average daily growth rate (d^{-1}) estimates in each eddy (noted μ(FDC) in section 4.2), is used as an indication of relative grazing pressure between eddies. This represents the fraction of newly produced cells that are lost by grazing and should therefore be compared to 1 to understand if cells can accumulate in eddies (g:μ<1 equivalent to g<μ).

4.4 Estimation of N_2 fixation and P-requirements of diazotroph populations

We combined the observations of daily integrated diazotroph biomass $\overline{B(t)}$ (μg C L^{-1}) with intrinsic growth rates μ(FDC) (d^{-1}) to determine the C production of each population over time.

Uncertainties in biomass and biological rates are discussed separately in their respective sections and reported in Table S4. Carbon was then converted into N and P, using literature values of taxa-specific stoichiometry (Table 2), to estimate P- (nmol P L^{-1} d^{-1}) and N-requirements (nmol N L^{-1} d^{-1}). We assume that N_2 fixation is the sole form of N acquisition for diazotrophs; thereby, estimates of N-requirements are equivalent to N_2 fixation rates.

(11) P-requirements (t) $= \int_0^t \frac{dP}{dt} = \frac{10^3}{12 \times C{:}P} \times \int_0^t \frac{dB}{dt} = \frac{10^3}{12 \times C{:}P} \times \mu(FDC) \times \overline{B(t)}$

N-requirements (t) $= \int_0^t \frac{dN}{dt} = \frac{10^3}{12 \times C{:}N} \times \int_0^t \frac{dB}{dt} = \frac{10^3}{12 \times C{:}N} \times \mu(FDC) \times \overline{B(t)}$ (N_2 fixation rates)

The intrinsic growth rates μ(FDC) were derived from the detection of dividing cells/filaments in populations of *Trichodesmium*, *Richelia*, *Calothrix*, and large *Crocosphaera* imaged by the IFCb. Since small *Crocosphaera* cells can not be imaged using the IFCb, we approximated their growth rates based on the log-difference in net abundance over time measured by the SeaFlow. Growth rates of UCYN-A could not be estimated since the small sublineage of the UCYN-A/haptophyte symbiosis dominant at Station ALOHA (UCYN-A1, Turk-Kubo et al. 2017) is too small to be detected by the IFCb and is conflated with other photosynthetic picoeukaryotes measured by the SeaFlow. However, a complementary study by Gradoville et al. (*in review*) measured single-cell NFRs by UCYN-A1 from the 2018 $^{15}N_2$ in situ array experiments using nanoscale secondary ion mass spectrometry (nanoSIMS). We combined these cell-specific rates with UCYN-A1 *nifH* gene abundances to estimate the contribution of UCYN-A1 to bulk N_2 fixation. It should be noted that these estimates include many potential sources of error, including possible discrepancies between *nifH* gene abundances and cell concentrations which we were not able to assess, as well as dilution of the heavy ^{15}N isotope through sample preparation prior to nanoSIMS measurements (Meyer et al. 2020).

5. Metatranscriptomic analyses

5.1 Diazotroph expression of P-stress marker genes

Following the predictions of abiotic factors controlling diazotroph limitations in eddies (Section 4.1), we investigated transcriptional regulation of P-stress marker genes during the 2017 cruise.

455 Metatranscriptome samples were collected from 15 m depth at ~4 h intervals for three days during the
456 Lagrangian sampling of the cyclonic and anticyclonic eddies (n=18 for each eddy). Seawater was collected
457 using Niskin® sampling bottles attached to the CTD rosette and 1 L was filtered onto 0.2 µm Supor®
458 Membrane Disc filters (Pall) housed in Swinnex™ units (MilliporeSigma) using a peristaltic pump. The
459 filtration time ranged from 15 to 20 min. Immediately following filtration, filters were placed in RNALater
460 (Invitrogen, Waltham, MA, USA) and stored at -80°C until processing.

461 RNA extractions were performed by first removing RNALater (via centrifugation and pipetting),
462 adding 300 μL of Ambion denaturing solution directly onto the filter, spiking in External RNA Controls
463 Consortium (ERCC) ExFold RNA Spike-In Mixes (Mix #1, 4456739, Invitrogen), and vortexing for 1 min.
464 Next, 750 μL of nuclease-free water was added to the sample and the samples were purified and DNase-
465 treated using a Chemagen MSM I instrument with the tissue RNA CMG-1212A kit (PerkinElmer).
466 Samples were enriched for mRNA by removal of rRNA using Ribozero (Illumina, San Diego, CA, USA).
467 The quality of purified RNA was assessed using Fragment Analyzer high sensitivity reagents (Agilent,
468 Santa Clara, CA, USA) and quantified using Ribogreen (Invitrogen). Next, cDNA was synthesized, and
469 sequencing libraries were produced using the ScriptSeq v2 RNA-Seq kit (Illumina #SSV21124). Unique
470 single-plex barcodes were annealed onto cDNA fragments during the PCR enrichment for Illumina
471 sequencing primers over 12 cycles, following the manufacturer's guidelines. Libraries were normalized to
472 4 nmol L^{-1} final DNA concentration, pooled in equal volumes, and sequenced using an Illumina® NextSeq
473 500 system with a V2 high output 300 cycle reagent kit. A phiX quality control (Illumina) reagent was
474 added to an estimated final contribution of 5% of the total estimated sequence density. A total of ~2
475 million, 150 bp paired-end reads were produced for each sample.

476 Sequence reads were verified and screened for quality using BBMap (v38.73) to remove adapters
477 and phiX, BFC (r181, Li 2015) to correct sequencing errors, and Trimmomatic (v0.39, Bolger et al. 2014)
478 to remove low quality bases. Raw sequence reads were submitted to the NCBI SRA under project number
479 PRJNA596510. Cleaned reads were assembled using RNA-SPAdes (v3.13.2, Bushmanova et al. 2019) and

480 genes were predicted from assembled transcripts using Prodigal (v2.6.3, Hyatt et al. 2010). A combined
481 gene database was created using the ALOHA 2.0 gene catalog (Luo et al. 2020) and CD-HIT (v4.8.1, Fu et
482 al. 2012) was used to dereplicate at 97% amino acid identity. Transcripts were identified and counted by
483 mapping cleaned reads against this combined gene catalog using BWA-MEM (v0.7.17,
484 www.github.com/lh3/bwa). Transcript counts were normalized to the ERCC standards to account for any
485 methodological biases among samples, including library preparation and sequencing. Counts were also
486 normalized to the volume of water filtered for each sample, to estimate transcripts per mL for each gene.
487 To use the ERCC spike-in as an internal standard in each sample, the correction factor was calculated as
488 follows: For each ERCC standard, the known quantities of spiked-in RNA standards were compared to
489 those same standard's read counts recovered by read mapping using BBMap (v38.73,
490 www.sourceforge.net/projects/bbmap/). A standard curve was generated for each sample, and the
491 corresponding correction factor calculated as the slope of the best fit line going through these pairs of
492 values with the intersection forced to the origin. The detection limit corresponded to the lowest molar
493 amount of the ERCC sequence detectable in each sample. Values above detection limits were further
494 normalized to the total sample expression sum of each specific genus level annotation, using GTDB (Parks
495 et al. 2018) for prokaryote transcripts. This step was required in order to compare eddy differential gene
496 expression based on cellular regulation rather than based on the total number of cells.
497 Several genes related to phosphorus transport and/or acquisition (reviewed by Stenegren 2020)
498 were extracted from the dataset according to KEGG annotation. Some of these gene transcripts
499 demonstrated diel expression patterns. To account for the expression periodicity and evaluate the
500 differences in gene transcript abundances between eddies, we standardized the abundance of transcripts
501 above detection limits within each eddy to the overall average of each gene transcript, computed from the
502 entire dataset (time points with undetected gene transcripts were excluded from this analysis). This step
503 allowed us to account for the large differences (i.e. several orders of magnitude) observed between baseline
504 expression levels of different gene transcripts. The statistical significance of the relative change in

expression was tested using a Kruskal-Wallis test (R function 'kruskal.test'). All gene transcripts from UCYN-A and *Calothrix*, as well as the transcripts of several genes from *Richelia* and *Trichodesmium*, were excluded from analyses as their abundances always fell below the detection limit in at least one eddy.

5.2 Estimation of protist community distribution using 18S rRNA

Following the identification of putative grazers of diazotrophs in eddies (Section 4.3), we analyzed the 18S rRNA signal from the top 10 protists during the 2016 and 2017 cruises. Eukaryotic metatranscriptomic samples (20 L) were collected in replicate every day at ~14:00 local time during the 2016 (25 m depth, n=2 in the anticyclone, n=3 in the cyclone) and 2017 (15 m depth, n=3 for each eddy) cruises using Niskin® sampling bottles attached to the CTD rosette. Samples were first prescreened through a 200 μm Nylon® mesh then filtered onto two 5 μm polycarbonate filters (47 mm) using a peristaltic pump.

Total RNA was extracted from individual filters after Harke et al. (2019) using a Qiagen RNeasy Mini Kit modifying the lysis step with the addition of Biospec 0.5 mm zirconia/silica beads. Briefly, lysis buffer and beads were added to each filter set (n=2), vortexed for 1 min, placed on ice for 30 s, and vortexed again for 1 min. Resulting lysate was pipetted and pooled into a single 5 mL tube. The rest of the Qiagen RNeasy Mini Kit protocol was then followed according to the manufacturer's instructions, adjusting volumes accordingly and incorporating the on-column DNase digestion step, using a Qiagen RNase-free DNase kit. Resulting total RNA was then eluted with RNase-free water and purified and concentrated with a RNeasy MinElute kit according to the manufacturer's instructions. Quantity and quality of extracted total RNA was assessed on an Agilent 2100 Bioanalyzer.

The extracted samples were split into two equal volumes of total RNA where one volume was sequenced directly (herein referred to as "unselected reads") for the community diversity analysis used in this study. Illumina® TruSeq libraries were sequenced with an Illumina HiSeq 2000 targeting 60 million paired-end reads, at the JP Sulzberger Columbia Genome Center, following Center protocols. These environmental sequence data are deposited in the Sequence Read Archive through the National Center for

530 Biotechnology Information under accession no. PRJNA515070. Raw sequence quality was visualized
531 using FastQC (www.bioinformatics.babraham.ac.uk/projects/fastqc/) and then cleaned and trimmed using
532 Trimmomatic (Bolger et al. 2014) v0.27 (paired-end mode, 4-bp-wide sliding window for quality <15,
533 minimum length of 2-bp).

534 Unselected reads were analyzed using RiboTagger (Xie et al. 2016) which uses a position-specific
535 scoring matrix to scan all rRNA reads to detect sequences next to the V4 region of 18S rRNA (Silva
536 version 119; Quast et al. 2013) reporting 33 nucleotide tag V4 region sequences downstream of the PSSM
537 matched position. Resulting alignment tables of these expressed rRNA tags (herein called 'ribotags') were
538 trimmed to remove ribotags with no SILVA annotation and ribotags aligning to metazoa or plastids prior to
539 normalization. The resulting trimmed datasets were normalized by rarefaction using the R function
540 'rarefy'. Ribotags without genus identification were labeled as 'unidentified' and the next highest
541 taxonomic identification level was used. The 10 most abundant ribotags were grouped by hierarchical
542 cluster analysis and an arbitrary cut of 3 clusters was fixed to identify which taxa consistently displayed a
543 relative increase, relative decrease, or inconsistent patterns in ribotag count in cyclones and anticyclones.
544

545 **Results & Discussion**

546 Mesoscale eddies add heterogeneity to the biogeochemistry and microbial community structure at
547 Station ALOHA (Barone et al. 2019), but the effects of eddies on N_2 fixation are not fully understood.
548 Sampling pairs of eddies in spatial proximity provides a unique opportunity to explore the effects of eddy
549 polarity on diazotrophy independent of seasonal changes, complementing the Eulerian approach of
550 previous NPSG analyses (Church et al. 2009; Böttjer et al. 2017). We also surveyed the spatial variability
551 of diazotroph abundances within eddies, which is not well resolved by the ~monthly measurements of the
552 HOT program at Station ALOHA. We present observations of N_2 fixation (Section 1.1) with
553 environmental context from three cruises in the NPSG (Section 1.2). We then compare NFRs and
554 diazotroph abundances observed in eddies to historical data from the HOT program (Section 1.3). Surface

rates and abundances are reported in Tables 4-5. Finally, we present evidence for three non-exclusive mechanisms through which eddies affect diazotrophy—the physical accumulation of diazotroph cells, bottom-up control, and top-down control—using fine-scale datasets and population models (Section 2). Model predictions are reported in Table S3 and detailed hereafter.

1. NFRs, *nifH* gene abundances, and environmental conditions on the three eddy cruises

Observations were carried out on three cruises to the NPSG, all of which sampled a cyclonic eddy and an anticyclonic eddy in open-ocean, oligotrophic waters north of the Hawaiian Islands (Fig. 1). These eddies varied by age and phase (defined by the fluctuations of SLA amplitude in the eddy centers) at the time of sampling (Table 1). In the 2017 and 2018 cruises, the anticyclones were in a stable phase and the cyclones were in a weakening phase. In the 2016 cruise, the anticyclone was intensifying and the cyclone was stable. The 2016 cruise sampled N_2 fixation rates, *nifH* gene abundances, and environmental conditions in the center of each eddy and at a frontal station between eddies. The 2017 and 2018 cruises both included intensive sampling within the center of each eddy (including NFRs, *nifH* gene abundances, IFCb abundances, and environmental conditions); the 2017 cruise also included a high-resolution sampling transect between the eddies.

1.1 Effects of eddy polarity and phase: elevated NFRs in stable anticyclones

The highest NFRs were observed in the anticyclones during the 2017 and 2018 cruises (Fig. 2). In both cruises, rates were measured using seawater collected from six depths (5-125 m) and incubated on free-floating, in situ arrays. There were strong differences in NFRs between eddies during the 2017 cruise: depth-integrated rates were ~6 times higher in the anticyclonic eddy (670 μmol N m^{-2} d^{-1}) than in the cyclonic eddy (115 μmol N m^{-2} d^{-1}). This range in NFRs between eddies, sampled 5 days and ~2° latitude apart, exceeds the range in monthly mean NFRs from the HOT program (~100-400 μmol N m^{-2} d^{-1}, Böttjer et al. 2017). During the 2018 cruise, depth-integrated NFRs were ~1.7-fold higher in the anticyclone (428 μmol N m^{-2} d^{-1}) than the cyclone (240-267 μmol N m^{-2} d^{-1}) (Fig. 2). Both anticyclones were in a relatively stable phase compared to the 2017 and 2018 cyclones (Table 1).

During the 2016 cruise, NFRs were highest in the cyclonic eddy (Figs. 2, S1). On this cruise, NFRs were measured at 25 m only via daytime and nighttime deck-board incubations. Daily NFRs in the cyclonic eddy were ~1.5 times higher than in the anticyclone and ~3 times higher than at the frontal station (Fig. 2). Care should be taken when comparing rates from the 2016 cruise to those from the 2017 and 2018 cruises, and to HOT observations (Section 2), because of the different methodologies used. Light and/or temperature may have differed in the deck-board incubators (used during 2016 only) compared to in situ conditions of the free-floating arrays (used during 2017, 2018, and HOT cruises). A previous comparison of NFRs measured using deck-board incubators versus in free-floating in situ arrays reported slightly (~15%) higher rates in the incubators (Wilson et al. 2012). The length of $^{15}N_2$ incubations also differed between the 2016 cruise (6-10 h daytime and nighttime incubations) and the subsequent cruises (24 h). Integrating hourly rates may have biased the 2016 daily NFR estimates due to the different diurnal patterns of N_2 fixation by diazotroph taxa (Wannicke et al. 2018; White et al. 2020); however, we consider this method acceptable since rates were measured for the majority of the 24 h period.

Our observation of higher rates in anticyclones than cyclones on two out of three cruises agrees with previous reports from the North Pacific (Fong et al. 2008; Wilson et al. 2017), Indian Ocean, Eastern South Pacific, and South China Sea (Holl et al. 2007; Löscher et al. 2016; Liu et al. 2020). However, the opposite trend was observed during the 2016 cruise, with the highest NFRs in the cyclonic eddy. Interestingly, the highest NFRs measured on all three cruises occurred within stable eddies, as the 2017 and 2018 anticyclones and 2016 cyclone all displayed small fluctuations of SLA in eddy centers (Table 1). Additional observations and future expeditions tracking specific eddies through their lifetime will be needed to confirm this trend. Nonetheless, our observations show that eddy polarity alone is not a robust predictor of NFRs, in agreement with the low correlation between corrected sea level anomalies and NFRs measured at Station ALOHA between 2012-2019 (Spearman correlation, r=0.08, *p*-value=0.58, n=48). The correlation remained non-significant during the months (April, May and July) and seasons (spring and summer) of the eddy cruises, but it should be noted that the number of observations (n~12 for seasonal

correlation and n~4 for monthly correlation) was lower than the sample size recommended (n=25) by Bonett and Wright (2000). Using a similar approach from 1993-2015, Barone et al. (2019) highlighted a significant link between eddy polarity and several biogeochemical factors promoting N_2 fixation, suggesting that environmental perturbations should be measured in concert with NFRs and diazotroph abundances in order to understand the role of eddies in shaping diazotrophy.

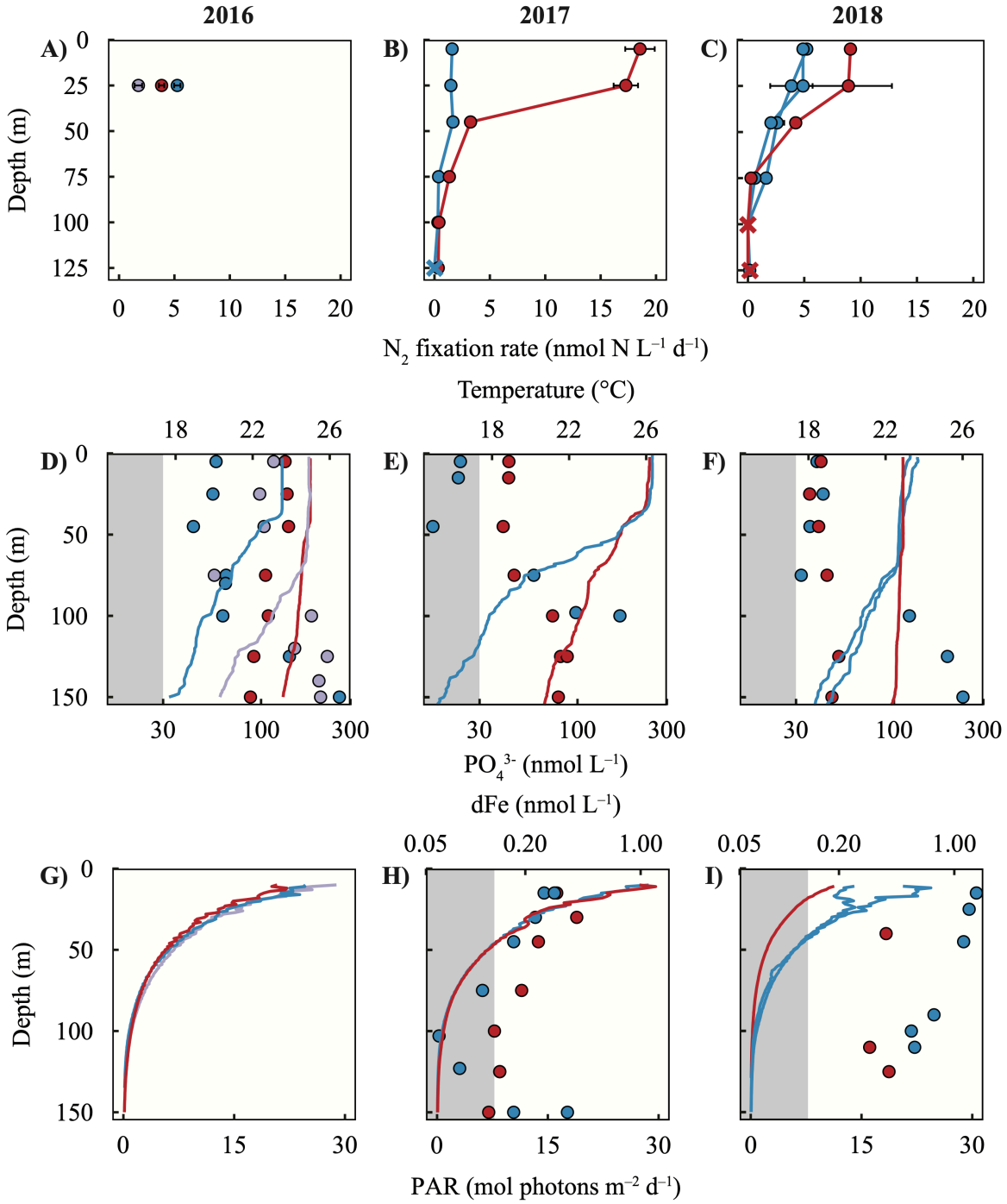

Figure 2: Depth profiles of N_2 fixation rates (A-C) and environmental gradients (D-I) during the 2016 (left), 2017 (middle), and 2018 (right) cruises. Red and blue indicate observations from the anticyclonic and cyclonic eddies, respectively (note that N_2 fixation rates were measured twice within the 2018 cyclone). × represent rates below detection limits. Purple in panels A, D, and G represents observations from a reference station between eddies (2016 only). Profiles of temperature (D-F, lines) and daily-integrated scalar PAR (G-I, lines) are shown on days and locations of the N_2 fixation measurements; PO_4^{3-} (D-F, circles) and dFe concentrations (G-I, circles) were measured at nearby stations within the same eddy. Gray rectangles in panels D-I indicate the threshold for severe P-limitation of diazotrophs reported by Letelier et al. (2019) and the corresponding threshold for severe Fe-limitation calculated using cell stoichiometry (Table 2). dFe data are not available for the 2016 cruise and potentially contaminated samples at 90 and 120 m were removed from the 2018 anticyclone profile.

1.2 Eddy polarity, environmental conditions, and NFRs: elevated rates in anticyclones linked to elevated PO_4^{3-}

Mesoscale eddies can affect light, temperature, and nutrient concentrations within the euphotic zone (McGillicuddy and Robinson 1997; Benitez-Nelson et al. 2007). Since these factors are all related to NFRs and diazotroph abundances (Luo et al. 2014), we examine each of these controls and how they varied between eddies on the three cruises.

Light and temperature are primary ecological controls for cyanobacterial diazotrophs: NFRs generally increase with both light and temperature (Luo et al. 2014), and taxa have unique light affinities and different optimal temperatures for growth (Table 3). Eddy dynamics can directly affect sea surface temperature (isopycnal uplift often resulting in cold core cyclones, McGillicuddy and Robinson 1997) and light attenuation (via nutrient injection leading to particle formation, Benitez-Nelson et al. (2007)). In this study, we compared light and temperature to NFRs in the surface ocean, since below the mixed layer rates rapidly decreased and showed non-significant differences between eddies (Fig. 2). We observed small

differences in mixed layer light and temperature between cyclonic and anticyclonic eddies during all three cruises. Additionally, when differences were observed between eddies, NFRs were inversely related to both parameters: sea surface temperature was lower in the 2016 cyclone and lower daily-integrated light was observed in the 2018 anticyclone due to cloud cover (Fig. 2). Thus, we discard the possibility that temperature or light drove the observed differences in NFRs between eddies.

Diazotrophs in the NPSG oscillate between P and Fe limitation (Letelier et al. 2019), shaped by taxa-specific P and Fe stoichiometry (Table 2) and uptake affinities (Table 3). Nutrient concentration ratios, reported in Table S1, also affect diazotrophs through resource competition, whereby fast-growing, non-diazotrophic phytoplankton outcompete diazotrophs under high N:P and/or N:Fe supply ratios (Ward et al. 2013). The uplift of isopycnals in cyclonic eddies can inject N, P, and Fe into the lower euphotic zone, where most of these nutrients are rapidly assimilated by the plankton community (McGillicuddy and Robinson 1997). Conversely, isopycnal downwelling in anticyclonic eddies can result in extreme N-depletion in surface waters, which has previously been used to explain observations of high NFRs in a NPSG anticyclone (Wilson et al. 2017).

In the present study, we observed a pattern of higher surface PO_4^{3-} concentrations in all three anticyclones. Thus, elevated PO_4^{3-} concentrations could have been linked to the higher NFRs observed in 2 out of three cruises. The lower euphotic zone (100-150 m) had higher PO_4^{3-} concentrations in cyclones, reflecting eddy-induced isopycnal uplift and depression in the cyclones and anticyclones, respectively (McGillicuddy and Robinson 1997; Church et al. 2009; Barone et al. 2019) (Fig. 2). However, the opposite pattern was observed at the surface, with PO_4^{3-} concentrations at 5 m of 134, 43, and 41 nmol L^{-1} in anticyclones and 58, 24, and 39 nmol L^{-1} in cyclones during the 2016, 2017, and 2018 cruises, respectively (Fig. 2). This observation is consistent with a recent analysis by Barone et al. (2019), which showed that decreases in SLA (characteristic of cyclonic eddies) at Station ALOHA are generally linked to a significant depletion in surface PO_4^{3-} concentrations. In our study, surface PO_4^{3-} in all eddies during the 2017 and 2018 cruises fell below 50 nmol L^{-1}, the empirical threshold for P-limitation of diazotrophs in the NPSG,

while surface PO_4^{3-} in the 2017 cyclone fell below 30 nmol L^{-1}, the apparent threshold for severe P-limitation (Letelier et al. 2019). As a consequence of higher PO_4^{3-} concentrations in anticyclones, surface inorganic N:P ratios were consistently lower in anticyclones than cyclones for all three cruises (Table S1), potentially promoting the elevated NFRs observed in 2017 and 2018 (Ward et al. 2013; Landolfi et al. 2015). It should be noted that all ratios were well below Redfield stoichiometry (N:P <1, Table S1), which has been chronically observed at Station ALOHA (Karl et al. 2001; Böttjer et al. 2017).

Dissolved Fe concentrations (available for 2017 and 2018 cruises only) did not fall below the apparent Fe-limitation threshold for diazotrophs (~0.18 nmol L^{-1}) determined using cell stoichiometry (Table 2) and the threshold for severe P-limitation (Letelier et al. 2019). For the 2017 cruise, dFe in the mixed layer was slightly higher in the anticyclone (~0.36 nmol L^{-1}) than in the cyclone (0.26 nmol L^{-1}), consistent with upwelling of low Fe waters from the lower euphotic zone in the NPSG (Fitzsimmons et al. 2015). In both eddies, comparison of particulate Fe:C ratios from 15 m (>100 μmol Fe:mol C) to those of *Crocosphaera* and *Trichodesmium* cultures (Table 2) suggest Fe-replete conditions (Table S1). While dFe in the mixed layer of the 2018 anticyclone (0.39 nmol L^{-1}) was similar to the 2017 eddies, dFe in the 2018 cyclone was 1.2 nmol L^{-1}, which is abnormally high for Station ALOHA (Fitzsimmons et al. 2015). Considering that Fe concentrations in Hawaiian coastal waters can be 1,000-fold greater than in open ocean waters (Hawco et al. 2020b), and that the trajectory of the cyclonic eddy intersected (and then deflected off) the Maui shelf one month before sampling (data not shown), it is likely that coastal Fe input led to the elevated dFe in this eddy. This natural Fe addition experiment did not lead to elevated NFR, implying that dFe was also not a limiting factor for diazotroph growth in 2018, consistent with the nutrient limitation thresholds proposed by Letelier et al. (2019).

1.3 Anomalies in NFRs and diazotroph abundances in the context of HOT observations: potential role of *Crocosphaera*

The >30 year HOT program at Station ALOHA provides critical insight into the seasonal and interannual dynamics of microbial processes in the NPSG (Karl and Church 2014). These data show a

seasonal pattern in surface ocean NFRs, with the highest rates occurring in late summer and early fall months (Fig. 3; Böttjer et al. 2017). Most previous observations of high NFRs associated with positive SLA at Station ALOHA have been at this time of year, when sea surface temperatures are at their highest (Church et al. 2009). The seasonality of NFRs likely reflects the seasonal succession of diazotrophs at Station ALOHA: abundances of *Trichodesmium*, *Crocosphaera*, and DDAs peak in the summer or early fall, while abundances of UCYN-A1 are high throughout the year with a peak during the spring (Fig. 3; Church et al. 2009; Böttjer et al. 2014).

Using HOT data as seasonal context, we found that anomalously high NFRs occurred in anticyclonic eddies during our spring (2018) and summer (2017) cruises. Rates in the 2017 and 2018 anticyclones greatly exceeded the highest monthly rates from previous observations (Fig. 3). While the HOT program often samples eddies passing over Station ALOHA, samples are rarely collected from the centers of eddies with as high and low of SLA as the eddies sampled in this study (Fig. 1, Barone et al. 2019). Our data suggest that anticyclones sometimes promote anomalously high NFRs in eddy centers. These anomalies and the variability of NFRs between eddies are likely linked to diazotrophic community structure. We estimated diazotroph abundances by quantifying the *nifH* genes of eight diazotroph taxa (Table 4, Fig. S2). To ensure that the variability in *nifH* gene abundances observed across mesoscale eddies was not due to a change in polyploidy (Sargent et al. 2016), variable DNA extraction efficiency, and/or other methodological biases, we compared the surface *nifH* genes copies with underway cell abundances of *Trichodesmium*, *Calothrix*, *Richelia*, and *Crocosphaera*, measured by automated flow cytometry within the 2017 and 2018 eddies (Fig. S5). While not meant to provide an estimate of the number of gene copies per cell, the comparison shows a strong relationship between genes and cell counts, with respective R^2 values of 0.71, 0.96, 0.89, and 0.91 and slopes of 8.2, 1.5, 2.5 and 1.9 *nifH* genes cell^{-1} (Supplementary Text S2).

Our observations are generally consistent with the seasonality of diazotrophs at Station ALOHA: of the diazotroph taxa quantified, UCYN-A1 had the highest *nifH* gene abundances during the spring (2016

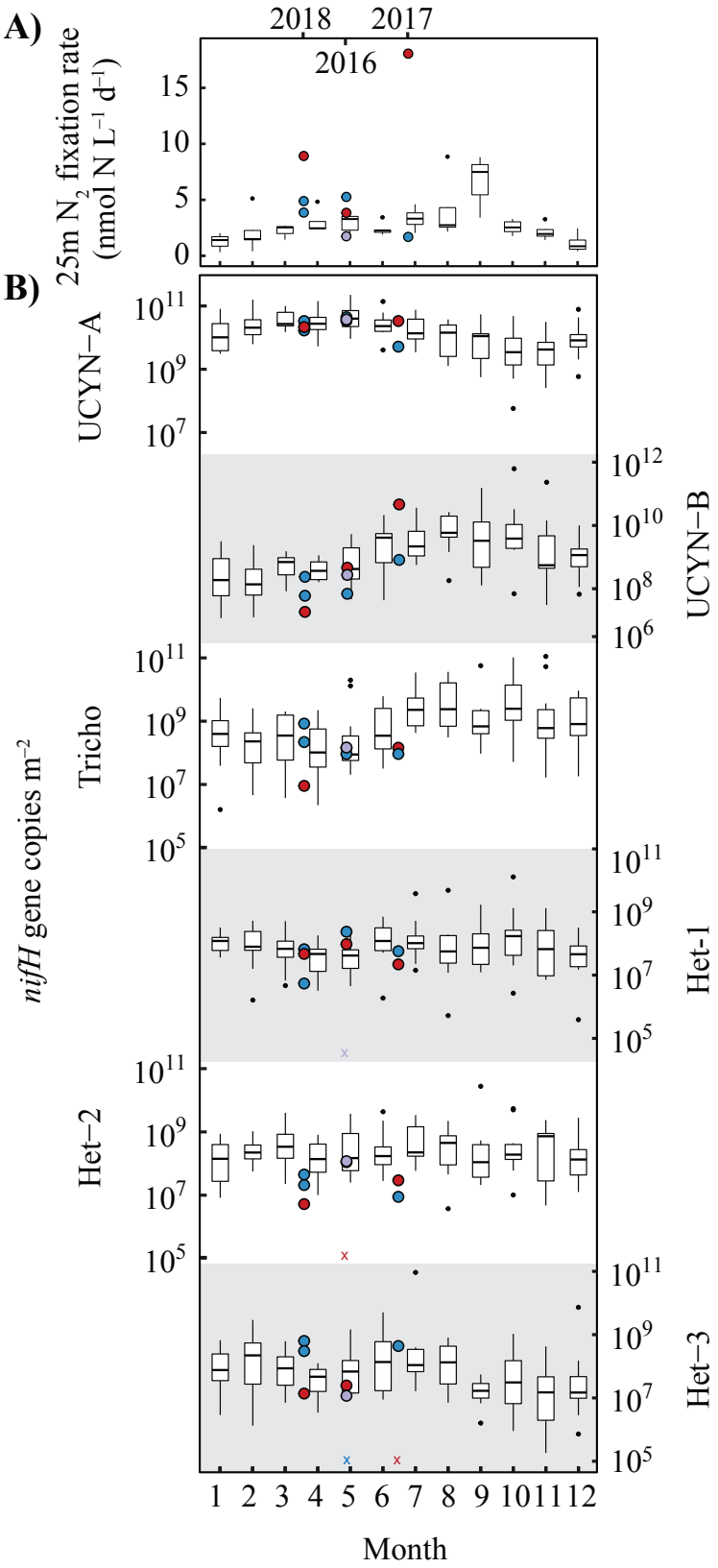

Figure 3: Eddy observations (colored circles) of N_2 fixation rates at 25 m depth (A) and depth-integrated (0-125 m) *nifH* gene abundances (B) superimposed on historical HOT data. Boxplots illustrate ~monthly measurements observed at Station ALOHA from 2012-2019 for N_2 fixation rates (Böttjer et al. 2017) and from 2004-2017 for qPCR-derived *nifH* gene abundances (Church et al. 2009, dataset doi: 10.5281/zenodo.4477269). Medians are shown as thick horizontal lines, 25-75% quantiles as boxes, the minimum and maximum values (up to 1.5 times the interquartile range) as whiskers, and outliers as black dots. Colored circles represent observations from cyclones (blue), anticyclones (red), and a reference station between eddies (purple, 2016 only), measured during eddy cruises and plotted according to the month of sampling. Observations below detection limits are represented by colored × at the bottom of each subplot.

and 2018) cruises, while *Crocosphaera* and UCYN-A both had high abundances during the early summer (2017) cruise (Fig. 3). The high *Crocosphaera nifH*

713 gene abundances in 2017 coincided with the presence of both small and large sub-populations as imaged
714 by autonomous flow cytometry (Fig. S3), as opposed to the 2018 cruise where only large *Crocosphaera*
715 cells were observed (Fig. S4).

716 Despite the agreement between HOT and eddy observations, comparing diazotroph abundances to
717 bulk NFRs and eddy polarity reveals multiple discrepancies: anomalous NFRs were not always linked to
718 anomalous diazotroph abundances and several diazotrophs showed inconsistent patterns with eddy

719 **Table 4:** *nifH* gene abundances of diazotroph taxa on the three cruises. Top: depth-integrated abundances
720 (0-125 m); bottom: volumetric abundances at the surface (25 m for 2016 and 2018 cruises; 15 m for 2017
721 cruise). NA: data not available. BD: below detection limits. Tricho = *Trichodesmium*.

Eddy	***nifH* gene abundances**								
	UCYN-A1	**UCYN-A3**	**UCYN-B**	**UCYN-C**	**Tricho**	**Het-1**	**Het-2**	**Het-3**	**Units**
2016:									
Anticyclone	3.4×10^{10}	4.5×10^{8}	4.6×10^{8}	4.7×10^{7}	1.4×10^{8}	9.5×10^{7}	BD	2.5×10^{7}	copies m^{-2}
	2.8×10^{5}	7.7×10^{3}	7.0×10^{3}	BD	2.7×10^{3}	2.7×10^{3}	BD	3.3×10^{2}	copies L^{-1}
Cyclone	4.4×10^{10}	1.7×10^{8}	6.9×10^{7}	1.2×10^{7}	9.2×10^{7}	2.4×10^{8}	1.1×10^{8}	BD	copies m^{-2}
	9.0×10^{5}	3.9×10^{3}	1.5×10^{3}	2.3×10^{2}	1.2×10^{3}	5.0×10^{3}	1.1×10^{3}	BD	copies L^{-1}
Reference	3.7×10^{10}	1.0×10^{9}	2.7×10^{8}	1.4×10^{7}	1.5×10^{8}	BD	1.2×10^{8}	1.2×10^{7}	copies m^{-2}
	3.5×10^{5}	2.1×10^{4}	4.0×10^{3}	BD	2.4×10^{3}	BD	2.7×10^{3}	BD	copies L^{-1}
2017:									
Anticyclone	3.3×10^{10}	NA	4.6×10^{10}	2.0×10^{7}	1.5×10^{8}	2.2×10^{7}	3.0×10^{7}	BD	copies m^{-2}
	1.3×10^{4}	NA	1.1×10^{5}	1.3×10^{1}	1.0×10^{3}	5.1×10^{2}	BD	BD	copies L^{-1}
Cyclone	5.2×10^{9}	NA	8.1×10^{8}	BD	9.2×10^{7}	5.7×10^{7}	8.9×10^{6}	4.4×10^{8}	copies m^{-2}
	1.6×10^{4}	NA	5.1×10^{3}	BD	1.6×10^{3}	1.6×10^{3}	1.1×10^{2}	1.4×10^{2}	copies L^{-1}
2018:									
Anticyclone	2.2×10^{10}	5.7×10^{8}	1.9×10^{7}	4.5×10^{7}	9.0×10^{6}	4.7×10^{7}	5.2×10^{6}	1.4×10^{7}	copies m^{-2}
	3.1×10^{5}	9.0×10^{3}	2.4×10^{2}	4.3×10^{2}	8.5×10^{1}	9.7×10^{2}	2.3×10^{1}	2.2×10^{2}	copies L^{-1}
Cyclone (array 1)	3.3×10^{10}	3.8×10^{8}	2.4×10^{8}	1.4×10^{9}	2.2×10^{8}	6.6×10^{7}	4.5×10^{7}	6.3×10^{8}	copies m^{-2}
	3.9×10^{5}	3.3×10^{3}	4.2×10^{3}	1.4×10^{4}	5.9×10^{2}	5.3×10^{1}	6.1×10^{2}	5.6×10^{3}	copies L^{-1}
Cyclone (array 2)	1.7×10^{10}	3.8×10^{8}	6.0×10^{7}	1.3×10^{8}	8.4×10^{8}	5.4×10^{6}	2.1×10^{7}	3.0×10^{8}	copies m^{-2}
	3.4×10^{5}	1.0×10^{4}	1.8×10^{3}	1.3×10^{3}	3.8×10^{4}	3.3×10^{1}	1.5×10^{2}	3.4×10^{3}	copies L^{-1}

722

polarity. The 2017 anticyclone was our only observation of anomalously high diazotroph abundances accompanying high NFRs. During this cruise, UCYN-B (*Crocosphaera*) and UCYN-A1 had the highest *nifH* gene abundances of the groups quantified; both groups also had higher abundances in the anticyclone than in the cyclone (up to 1.4×10^6 and 6.2×10^5 *nifH* genes L^{-1} respectively, Fig. S2). Independent measurements of *Crocosphaera* biomass via flow cytometry likewise showed higher concentrations in the anticyclone (Fig. S3). Comparing our *nifH* observations to historical HOT data shows that *Crocosphaera* abundances in the 2017 anticyclone exceeded all previous measurements from the months of June and July, while abundances in the cyclone were below the seasonal mean (Fig. 3). In contrast, UCYN-A1 abundances in the anticyclone, though higher than abundances in the cyclone, were only slightly above the seasonal mean (Fig. 3). These data suggest that *Crocosphaera* likely played a major role in driving the high NFRs observed in the 2017 anticyclone. High *Crocosphaera* abundances have been recently linked to high NFRs in another anticyclonic eddy of the NPSG (Wilson et al. 2017). However, we observed the opposite pattern for this group during the 2018 cruise (higher *Crocosphaera* abundances in the cyclone), indicating an inconsistent relationship with eddy polarity. Since both anticyclones were stable in 2017 and 2018, eddy phase cannot explain this difference (Table 1). The relatively homogeneous vertical profiles of temperature, inorganic nutrients (Fig. 2), and oxygen (data not shown) in the upper 150 m of the 2018 anticyclone indicate a deep penetration of surface water in this eddy. While this phenomenon is fostered by the depression of surface isopycnals typical of anticyclones, it might have been enhanced by the relatively deeper winter mixing observed in anticyclonic eddies (Dufois et al. 2016; Gaube et al. 2019). We speculate that the latter mechanism could also explain why we measured lower *Crocosphaera* abundance in the anticyclone: if the seed population of *Crocosphaera* had been diluted to a larger extent by winter mixing in the anticyclonic eddy, we would have measured lower abundance in the anticyclone than in the cyclone under the assumption of equal growth rates in the two eddies (Fig. S8).

During the two springtime (2016 and 2018) cruises, UCYN-A1 was the most abundant diazotroph quantified. Abundances were higher in cyclones in both years, as opposed to the summer cruise where

higher abundances were observed in the anticyclone, suggesting that UCYN-A1 is not favored in eddies of specific polarity (Fig. 2, Fig. 3, Table 4). During the 2016 cruise, UCYN-A1 *nifH* gene abundances at 25 m were 2.5 and 3.2 times higher in the cyclone (9.0×10^5 *nifH* genes L^{-1}), where the highest rates were measured, than in the anticyclone and the frontal station (2.8 and 3.5×10^5 *nifH* genes L^{-1}, respectively) (Fig. S2). The only other groups with elevated abundances in the cyclone were Het-1 and Het-2, whose *nifH* gene abundances were also high compared to historical HOT data (Fig. 3, Fig. S2). Hourly NFRs were higher during the day than at night for all three stations, and the cyclonic eddy had the highest ratio of daytime to nighttime NFR (~11:1, Fig. S1), supporting the conclusion that UCYN-A1, Het-1, and/or Het-2 (all daytime N_2-fixers) drove the higher NFRs observed in the cyclonic eddy.

In contrast, during the 2018 cruise, anomalously high NFRs were observed in the anticyclone (Fig. 3), but the most abundant diazotroph quantified (UCYN-A1, maximum abundance of 6.2×10^5 *nifH* genes L^{-1}, Fig. S2), had similar abundances between eddies (Table 4, Fig. 3). The only quantified diazotroph with higher depth-integrated abundances in the anticyclone during the 2018 cruise was UCYN-A3, whose relatively low abundances (maximum 1.7×10^4 *nifH* genes L^{-1}) make it unlikely to be responsible for the high rates. There are several possible explanations for the mismatch between diazotroph abundances and NFRs in the 2018 eddies. Bottom-up control factors are not well understood for the uncultivated UCYN-A symbioses (Zehr and Capone 2020), but for the other diazotrophs, differences in cell-specific activity between eddies is unlikely to explain our observations (Fig. S8) since higher light, temperature, and dFe concentrations were observed in the cyclone where rates were lower (Fig. 2). It is possible that other resources, such as organic nutrients (Benavides et al. 2020), play a role in modulating NFRs between eddies. Alternatively, our ddPCR assays could be missing important diazotrophic taxa including non-cyanobacterial diazotrophs, whose importance in marine ecosystems are not well-understood (Moisander et al. 2017), or could misrepresent organismal abundances due to the confounding relationship between *nifH* gene abundances and cell concentrations (Table 2, Fig. S5). Finally, the enigmatic pattern observed in 2018 may be due to the patchiness of diazotroph communities. In 2018, replicate in situ arrays were deployed on

different days within the cyclonic eddy, revealing within-eddy fluctuations in NFRs (Fig. 2). Lagrangian sampling within eddy centers also demonstrated large fluctuations in filament detection of *Richelia* and *Calothrix* with the IFCb (Fig. S4), which could potentially drive observed fluctuations in N_2 fixation rates both within and between eddies during the 2018 cruise. Past Lagrangian surveys in NPSG eddies have revealed the spatiotemporal patchiness of *Trichodesmium* (Robidart et al. 2014) whose origin may be linked to fronts (wind stress mixing), temporal forcings (e.g. biological interactions), or organism behavior that remain to be explored (McGillicuddy and Franks 2019).

2. Mechanisms affecting N_2 fixation in NPSG eddies

The inconsistent relationships among eddy polarity, diazotrophic community structure, and NFRs observed here and elsewhere (Liu et al. 2020 and references therein) may be explained by the multiple mechanisms through which eddies influence diazotrophs. Here, we review these mechanisms and present evidence for their importance in driving our observations of anomalously high NFRs in anticyclones.

2.1 Eddy-driven physical accumulation: evidence from *nifH* gene distributions

Buoyant plankton can be concentrated in areas of surface convergence, where cells are horizontally advected to the site of convergence and then acted upon by the opposing forces of downwelling and the upward buoyant force (Yoder et al. 1994; D'Asaro et al. 2018). The buoyancy of diazotrophic taxa varies greatly: smaller diazotrophs (e.g. *Crocosphaera* and *Calothrix*) are negatively buoyant and sink at maximum respective rates of 0.35 and 0.07 m d^{-1} (Bach et al. 2012; Tuo 2015) while the large diazotrophs *Trichodesmium* and *Richelia-Rhizosolenia* have the ability to actively regulate their buoyancy via gas exchange and carbohydrate storage (Villareal and Carpenter 2003). As a result, a fraction of these populations may become positively buoyant and ascend the water column at rates of 70 ± 2 m d^{-1} (Walsby 1978) and 86 ± 43 m d^{-1} (Villareal and Carpenter 1989), respectively. Positively buoyant *Richelia-Hemiaulus* have been reported to ascend at lower rates (0.07-0.56 m d^{-1}), with buoyancy linked to the production of transparent exopolymer particles (Hoppe 2013). Elevated surface abundances of

Trichodesmium and *Richelia* have been observed at numerous frontal features (Yoder et al. 1994; Aldeco-Ramírez et al. 2009; Benavides et al. 2011; Guidi et al. 2012) and within anticyclonic eddies (Fong et al. 2008; Church et al., 2009).

Mesoscale vertical velocities are generally linked to the displacements of isopycnals during the formation and strengthening of eddies (McGillicuddy et al. 1998) which has led to the misconception that downwelling only occurs in anticyclones. In reality, vertical velocities are temporally and spatially dynamic and may switch direction over the lifetime of an eddy as a result of internal and external forcing (Pilo et al. 2018). For example, downwelling can occur in intensifying anticyclones and weakening cyclones (McGillicuddy 2016), cyclones under constant wind (Gaube et al. 2015), and at the cyclonic side of eddy fronts (Mahadevan 2016). The downwelling-induced physical accumulation of cells has been used to explain the occurrence of surface *Trichodesmium* slicks (Olson et al. 2015) and *Rhizosolenia* mats (Villareal and Carpenter 1989) in eddies of both polarities.

The fine-scale distribution of diazotrophs across the pair of adjacent eddies measured in 2017 shows evidence for the physical accumulation of *Trichodesmium* and *Richelia* (Fig. 4). The highest *nifH* gene abundances of *Trichodesmium* and *Richelia* were observed near the surface at the cyclonic side of the front separating the two eddies (Fig. 4B-C), consistent with accumulation via surface downwelling caused by frontal dynamics. A surface bloom of *Trichodesmium* was also visually observed at the cyclonic side of the front (148 ± 44 filaments mL^{-1} measured by the IFCb from bucket samples, Fig. 4B), likely also driven by frontal downwelling. These results are consistent with a previous survey of *Trichodesmium* in an eddy dipole of the NPSG, which also reported maximal abundances at the front between eddies (Guidi et al. 2012).

Our observations are insufficient for determining the importance of physical accumulation on NFRs across the full eddy-eddy transect. NFR measurements were conducted in the center of each eddy but not on the cyclonic side of the eddy-eddy front where *Trichodesmium* and DDAs appeared to be physically accumulated during the 2017 cruise. Thus, while the eddy-induced physical accumulation of large

diazotrophs likely explains elevated NFRs and abundances of large diazotrophs in some previous studies (Fong et al. 2008; Olson et al. 2015), our eddy observations were likely driven by the balance of bottom-up and top-down control pressures within eddies.

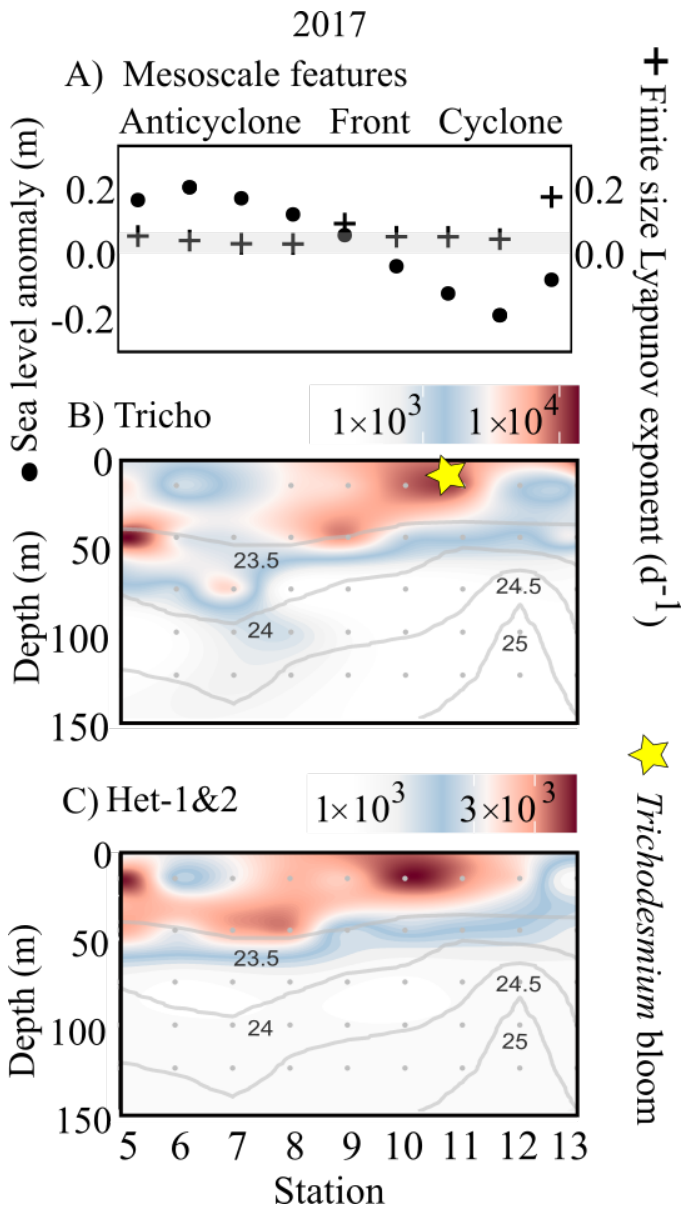

Figure 4: Eddy physical characteristics (A) and interpolated *nifH* gene abundances (B-C) across the high resolution 2017 eddy transect. Sea level anomalies (SLA, circles) and Finite-Size Lyapunov Exponent (FSLE, cross) mark the location of eddy centers (maximum in absolute SLA and null FSLE) and the front at station 9 (null SLA and maximum FSLE). The contours of potential density anomaly (kg m^{-3}) in B-C depict the vertical displacement of isopycnal surfaces associated with mesoscale eddies. The gray rectangle in A indicates the threshold of frontal filaments derived from the analysis of FSLE in the North Pacific Ocean (Guo et al. 2019). Cross-sections of *nifH* gene abundances suggest the physical accumulation of buoyant diazotrophs *Trichodesmium* (Tricho, B) and *Richelia* (Het-1/2, C) on the cyclonic side of the eddy-eddy front. A surface bloom of *Trichodesmium* (yellow star, positioned in the contour based on its latitude between Stations 10 and 11) was visually detected and sampled with imaging flow cytometry.

2.2 Eddy-driven bottom-up control: differences in growth rates linked to P-limitation

Our analysis of environmental conditions on the three eddy cruises identified surface PO_4^{3-} concentration as the primary bottom-up control factor explaining observed differences in NFRs between cyclones and anticyclones (Section 1.2), especially during the 2017 cruise, when we observed one of the highest bulk NFRs ever reported near Station ALOHA (Fig. 3). We investigated evidence for bottom-up control on individual diazotroph taxa in 2017 by (1) comparing estimates of growth rates via observations of mitotic fractions for specific diazotroph populations between eddies, both in situ and after nutrient amendment, (2) using in situ PAR, temperature, and nutrient concentrations to model growth rates and assess the limiting factor for each group, and (3) assessing diazotroph P-stress markers from transcriptomic data. We also discuss the contribution of individual populations to bulk NFRs resulting from cell-specific activity and biomass (the net effect of bottom-up and top-down control).

2.2.1 In situ growth rates and contributions to bulk N_2 fixation in mesoscale eddies

The in situ growth rates of large *Crocosphaera*, *Trichodesmium*, and DDAs during the 2017 cruise were estimated by following the fraction of dividing cells (filaments for DDAs) imaged with the IFCb (Fig. 5). These estimates represent the lower bounds of true population growth rates due to the sample aggregation required to count enough filamentous diazotrophs. The number of observations, daily fractions of dividing diazotrophs, and growth rates are reported in Table S4, along with their uncertainties (see Supplementary Text S1). Amongst diazotroph populations, *Crocosphaera* achieved the highest growth rates at the surface, with maximum average rates (0.84 ± 0.25 d^{-1}) ~three-fold greater than the growth rates of *Trichodesmium* (0.33 ± 0.05 d^{-1}) or DDAs (0.25 ± 0.22 d^{-1}). These rates, noted μ(FDC) in Table S3, were generally consistent with growth rate estimates of *Crocosphaera* and DDAs from previous field studies (Foster et al. 2011; Wilson et al. 2017) and with maximum growth rates measured in cultures of *Crocosphaera* (0.86 d^{-1}) and *Trichodesmium* (0.33 d^{-1}) (Table 3).

The contribution of each diazotroph group to bulk N_2 fixation (Table 5) was estimated by combining taxa-specific elemental stoichiometry (Table 2) with in situ growth rates and independent measurements of UCYN-A1 cell-specific NFRs from the 2018 cruise (Gradoville et al., *in review*).

Table 5. Diazotroph requirements and estimated contributions to surface bulk N_2 fixation rates and PO_4^{3-} uptake rates during the 2017 and 2018 cruises (Fig. S3-4). Individual requirements are derived from estimates of in situ growth rates during Lagrangian sampling combined with taxa-specific elemental stoichiometry (Table S4). Uncertainty related to biomass (20%) and rates (1-55%) are reported in Table S4. We assumed that N-requirements are only met through N_2 fixation. No Lagrangian sampling was conducted during the 2016 cruise.

			N_2 fixation rates in nmol N L^{-1} d^{-1} (Contribution to bulk N_2 fixation rate, %)					
Eddy	Date HST	Bulk rate	UCYN-A1[a]	*Crocosphaera*		*Trichodesmium*	*Richelia*	*Calothrix*
				Large	Small			
2017: Cyclone	07-06	1.48 ± 0.27	N.D	0.36 (24%)	0.04 (3%)	0.17 (11%)	0.23 (16%)	0.25 (17%)
Anti-cyclone	07-11	17.27 ± 0.13		10.25 (59%)	4.6 (26%)	0.20 (1%)	0.15 (1%)	0 (0%)
2018: Cyclone	03-29	3.86 ± 1.88	1.44 (37%)	0.41 (11%)	0.0 (0%)	0.52 (13%)	0.0 (0%)	0.06 (1%)
Cyclone	04-04	4.89 ± 0.14	1.76 (36%)	2.87 (59%)	0.0 (0%)	0.47 (10%)	0.07 (2%)	0.31 (6%)
Anti-cyclone	04-07	8.92 ± 3.86	1.18 (13%)	1.47 (17%)	0.0 (0%)	0.00 (0%)	0.0 (0%)	0.08 (1%)

			P-requirements in nmol P L^{-1} d^{-1} (Contribution to bulk PO_4^{3-}-uptake rate, %)				
Eddy	Date HST	Bulk rate >2 μm	*Crocosphaera*		*Trichodesmium*	*Richelia*	*Calothrix*
			Large	Small			
2017: Cyclone	07-04	0.31	0.06 (18%)	0.01 (3%)	0.032 (10%)	0.01 (3%)	0.001 (0.3%)
	07-05	0.32	0.04 (12%)	0.01 (3%)	0.025 (8%)	0.004 (1%)	0.000 (0%)
	07-06	0.33	0.01 (4%)	0.001 (0.3%)	0.020 (6%)	0.012 (4%)	0.013 (4%)
Anti-cyclone	07-09	0.83	0.51 (62%)	0.16 (19%)	0.036 (4%)	0.011 (1.3%)	0.03 (4%)
	07-10	1.00	0.47 (47%)	0.2 (20%)	0.036 (4%)	0.000 (0.0%)	0.03 (3%)
	07-11	0.90	0.42 (46%)	0.2 (22%)	0.023 (3%)	0.008 (0.8%)	0.00 (0%)

[a]Note that UCYN-A cell-specific NFRs may be underestimated due to potential dilution of the ^{15}N isotope through fixation and the CARD-FISH procedure. Applying the Meyer et al. (2020) correction factor for a positive CARD-FISH assay produces maximum possible UCYN-A cell-specific NFRs ~4-fold greater than those listed in this table (Gradoville et al., *in review*).

These estimates indicate that the small diazotrophs (*Crocosphaera* and UCYN-A1) had larger contributions to bulk NFRs, up to 85 and 37% respectively, than the large diazotrophs (*Trichodesmium* and DDAs), a common pattern at Station ALOHA (Church et al. 2009). In 2017, the contribution of *Trichodesmium,* up to 11%, fell below previous *nifH*-based predictions by Goebel et al. (2007) of 60-96% during summer and fall. This was expected since our estimates account for limitation other than light (e.g. nutrients and temperature) and more importantly, do not rely on *nifH* concentrations which may be biased by the high degree of polyploidy in *Trichodesmium* (Sargent et al. 2016, Fig. S5).

Diazotroph taxa displayed differences in growth rates and estimated contributions to NFRs between eddies. *Crocosphaera* in situ growth rates and contributions to bulk NFRs were significantly (*p*-value = 0.0003) higher in the 2017 anticyclonic eddy (0.84 ± 0.25 d^{-1}, 85% total contribution of small and large populations) than in the cyclonic eddy (0.63 ± 0.37 d^{-1}, 27%). This is consistent with the higher biomass of *Crocosphaera* observed in the 2017 anticyclone (Fig. S3) and suggests that cell division was limited in the cyclone. Differences in in situ growth rates between eddies were not significant for *Trichodesmium* (*p*-value = 0.84) or DDAs (*p*-value = 0.69). Compared to their maximum theoretical growth rates (Table 3), *Trichodesmium* appeared to grow optimally in either polarity while DDAs grew significantly slower in both eddies. Deck-board incubations after nutrient additions (+NO_3^-, PO_4^{3-}) relative to controls also suggested that *Crocosphaera* was nutrient-limited in the cyclone, DDAs were nutrient-limited in both eddies, and *Trichodesmium* was not nutrient-limited (Fig. S6). The lack of nutrient limitation for *Trichodesmium* may be due to mutualistic interactions within its microbiome (Gradoville et al. 2017), which may enable access to Fe reservoirs in dust particles (Basu et al. 2019) and scavenge P (Rouco et al. 2018).

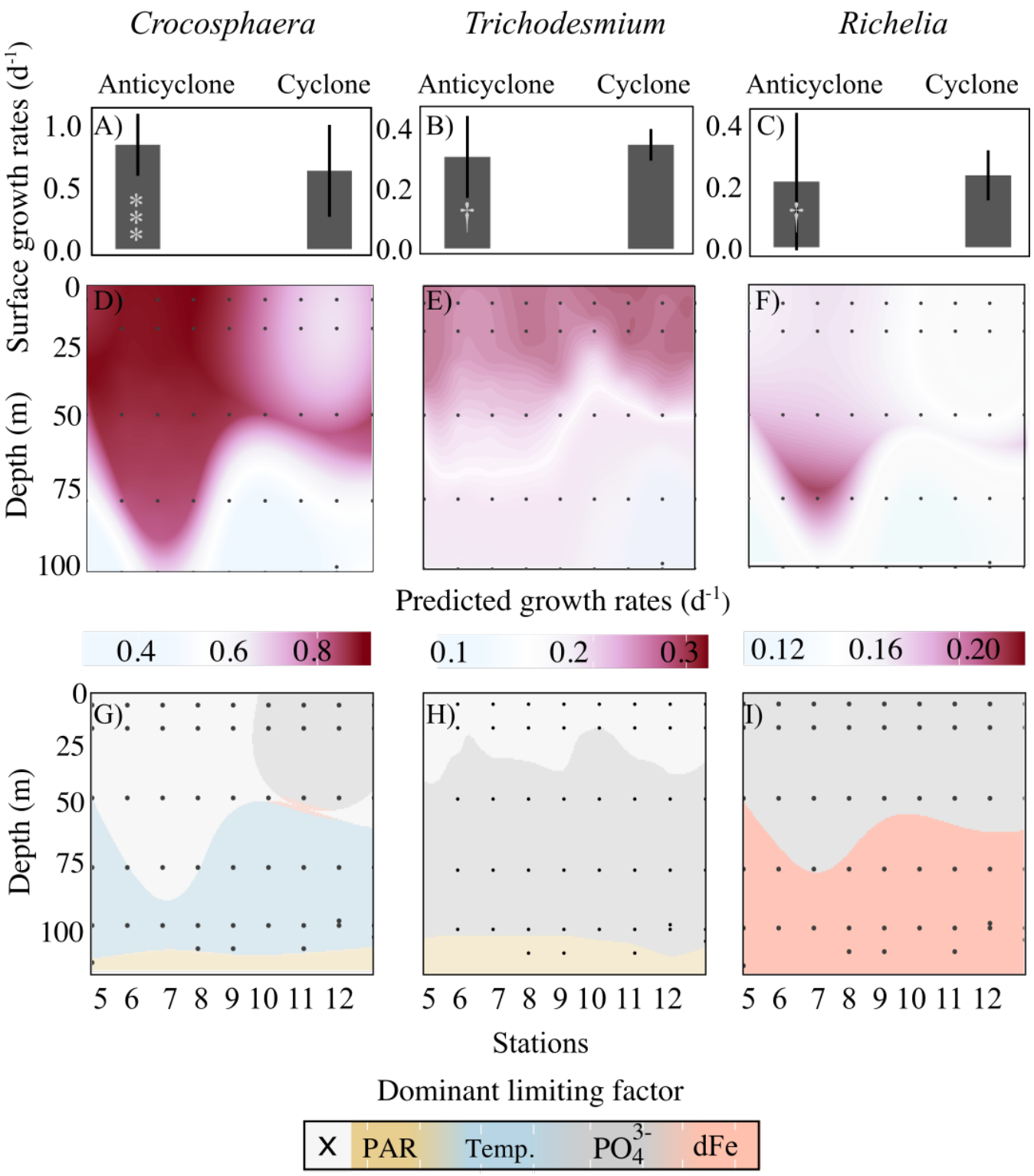

Figure 5: 2017 estimates of the growth rates and limiting factors for *Crocosphaera* (A, D, G), *Trichodesmium* (B, E, H), and *Richelia* (C, F, I). Diazotroph growth rates were measured in situ in each eddy center by following the fractions of dividing cells; bars and error bars represent the mean and standard deviation of growth rates among days within each eddy (A-C). Note the different scales in growth

rates for each population. Predictions of growth rates (D-F) and limiting factors (G-I) across the eddy transect are based on parameters provided in Table 3 combined with interpolated cross-sections of temperature (Temp.), average scalar irradiance (PAR), and inorganic nutrient concentrations (PO_4^{3-}, dFe). The locations of observations are indicated by black circles in D-I. Diazotrophs showed various limitations to the eddy-driven environmental gradients, including a strong P-limitation for *Crocosphaera* in the cyclone and P/Fe-limitation for *Richelia*. Note that the thermal adaptation of DDAs could not be parameterized, causing apparent maximum growth rates at depth where nutrients concentrations were highest (Fig. 2E-H). *P*-values: *** (<0.001); † (not significant).

2.2.2 Predictions and field-based evidence of P-limitation in mesoscale eddies

Surface predictions of the factors limiting the growth of *Crocosphaera*, *Trichodesmium*, and DDAs in response to eddy-driven environmental gradients, noted μ(T,E,PO_4^{3-},dFe) in Table S3, support our division-based growth rate measurements (Fig. 5G-I). All populations showed non-significant differences between the two growth rate estimates (Table S3). Modeled estimates of diazotroph growth rates and limiting factors are based on measured PAR, temperature, PO_4^{3-}, and dFe concentrations (Fig. 2) combined with taxa-specific adaptations measured in cultures (Table 3). In 2017, predicted growth rates of *Crocosphaera* and DDAs within the mixed layer were lower in the cyclonic eddy (Fig. 5D-F), due to low PO_4^{3-} concentrations (Fig. 2). Compared to *Trichodesmium,* both populations have low affinities to ambient PO_4^{3-} concentrations (Table 3). This resulted in the prediction of P-limitation in the cyclone for *Crocosphaera* and in both eddies for DDAs, while *Trichodesmium* was not limited (based on a limitation threshold arbitrarily set at 80% of the maximum theoretical growth rate of each taxa) (Fig. 5G-I). Adaptations of *Trichodesmium* to P-depleted environments include the utilization of dissolved organic P (DOP) (Dyhrman et al. 2006). Multiple strains of *Crocosphaera* and DDAs lack key genes involved in DOP scavenging (Dyhrman and Haley 2006), and thus rely more on PO_4^{3-}. Since DOP concentrations are generally similar between eddies with different polarities at Station ALOHA (Barone et al. 2019), the

higher PO_4^{3-} concentrations in anticyclonic eddies, observed in this study and more broadly in the NPSG (Robidart et al. 2014; Fitzsimmons et al. 2015; Barone et al. 2019), is likely a key factor allowing *Crocosphaera* to bloom within anticyclones. These blooms should be restricted to the surface, as our model predicted light and temperature limitation at depth (Fig. 5G-I).

In order to further investigate evidence for differential P-limitation between eddies during the 2017 cruise, we analyzed the expression of genes related to PO_4^{3-} and DOP acquisition and transport by diazotroph populations within the mixed layer (Fig. 6A-C). Expression of the latter by *Trichodesmium* did not differ between eddies, consistent with the lack of predicted nutrient limitation for this group in either eddy (Fig. 5). In contrast, several genes expressed by *Crocosphaera* and *Richelia* were significantly upregulated in the cyclone. These genes are commonly used as P-stress markers (Dyhrman and Haley 2006; Pereira et al. 2016) and we therefore would expect their expression to increase when cells are P-depleted. Thus, the elevated expression of P-stress markers observed for *Crocosphaera* and DDAs in the cyclonic eddy is consistent with P-limitation. These trends in gene expression matched the changes in PO_4^{3-}-uptake across eddies, measured by radiolabeled tracer (Fig. 6D). Measurements of >2 μm PO_4^{3-} uptake were higher in the anticyclone (30% of the total PO_4^{3-}-uptake) than in the cyclone (10% of the total PO_4^{3-}-uptake, data not shown). In comparison, this size fraction has been previously reported to account for 11 ± 0.05% of the total uptake at Station ALOHA under ambient conditions and 24 ± 21% when amended with additional PO_4^{3-} (Björkman et al. 2012). The estimated contribution of *Crocosphaera* to >2 μm PO_4^{3-}-uptake in the anticyclone was high (67-81%, Table 5), consistent with observed trends in biomass (Fig. S3) and P-stress transcript levels (Fig. 6). Together, these data suggest that reduction of P-limitation in the 2017 anticyclone led to increased rates of growth and N_2 fixation by *Crocosphaera*, contributing to the high measurement of bulk NFR.

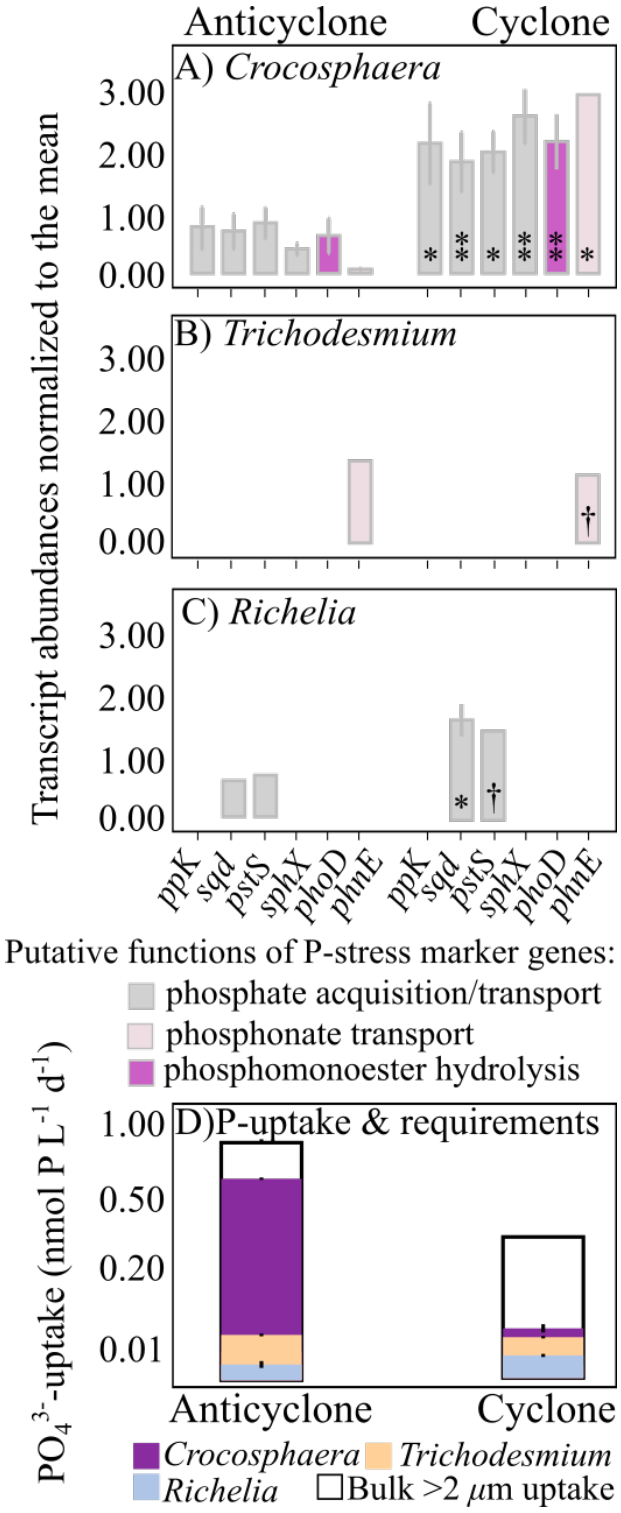

Figure 6: P-stress marker gene expression (A-C) and estimated P-uptake (D) of *Crocosphaera*, *Trichodesmium*, and *Richelia* within the mixed layer (15 m) in 2017. Note the log-scale for P-uptake rates. Panel D shows that bulk P-uptake in the >2 μm size-fraction (black) and individual estimates of P-requirements of *Crocosphaera* (purple) were high in the anticyclone, linked to the alleviation of P-limitation reflected in P-stress transcripts. Individual bars in A-C represent the average (± standard errors) standardized transcript abundances for each P-stress marker gene expressed in *Crocosphaera* (A), *Trichodesmium* (B), and *Richelia* (C). Fold-change in relative expression of P-stress marker genes indicates that cells upregulated the genes related to dissolved inorganic (*ppk, skd, pstS, sphX*) and organic (*phoD, phnE*) P acquisition/transport as a result of P-limitation in the cyclone. *ppK: polyphosphate kinase, sqd: sulfolipid biosynthase (substitution of P-lipids), pstS/sphX: high-affinity phosphate transporter, phoD: Alkaline phosphatase, phnE: phosphonate transporter. P*-values: ** (<0.005) * (<0.01) † (not significant)

2.3 Eddy-driven top-down control: differences in grazing pressure

While our results show that eddies modulate bottom-up control for diazotrophs, some taxa had small variations in surface growth rates between eddies compared to the observed differences in abundances. For instance, during the 2017 cruise, *Calothrix* average growth rates were only 4% different between eddies (Table S3), yet abundances were 2 to 4 orders of magnitude greater in cyclones (Table 4). This apparent discrepancy may be due to differences in loss terms between eddies. During 2017, the comparison between intrinsic and net growth rates (Fig. S6) suggest that top-down controls were significant for *Crocosphaera* (55% average difference between intrinsic and net growth rates) and relatively lower for *Trichodesmium* (30% difference). We used a predator/prey model to explore grazing rates (g) on specific diazotrophs in 2017 and 2018 (Fig. 7). Importantly, the estimates of diazotroph growth rates (r) fitted with the predator/prey model do not equal division rates measured by the fraction of mitotic cells, μ(FDC), suggesting that other losses must be accounted for to fully understand the role of eddies in shaping diazotroph top-down controls (Table S3).

2.3.1 Dichotomy between large and small diazotroph losses

There is increasing evidence that grazing is a significant loss term for small unicellular diazotrophs (Landry et al. 2008; Wilson et al. 2017) while losses of *Trichodesmium* are generally driven by viral lysis, as reviewed by Mulholland (2007). Visual inspection of *Trichodesmium* filaments from the bloom at the edge of the 2017 cyclone (Fig. 4) suggests that the main loss for *Trichodesmium* may have been programmed cell death or viral lysis (Berman-Frank et al. 2004; Hewson et al. 2004), as a majority of the filaments contained cells which were shrunken or lacking thylakoids (Fig. 7M). Additional sources of diazotroph cell loss (including viral lysis, programmed cell death, additional grazing by organisms not detected, vertical migration, mixing, and/or sinking) were not observed via independent approaches. We thus focus our discussion on modeled grazing, as we confirmed the interaction between diazotrophs and their putative predators via images of ingested prey (Fig. 7 D-L) and compared grazer growth rates from observations of dividing cells to model predictions (Fig. S7).

In the vicinity of Station ALOHA, Wilson et al. (2017) and Turk-Kubo et al. (2018) used the dilution method to measure bulk grazing rates of UCYN-B, UCYN-A, and UCYN-C. Grazing rates ranged from 0-100% of the daily growth rates of diazotrophs, indicating that grazers and/or viruses can grow as fast as their prey. Early reports have identified mesoplanktonic copepods grazing on *Trichodesmium* (O'Neil et al. 1996; O'Neil 1998; Azimuddin et al. 2016), UCYN-C (Hunt et al. 2016), UCYN-A (Scavotto et al. 2015), UCYN-B, and groups Het-1&2 (Conroy et al. 2017). More recently, small nano/microplanktonic flagellates (e.g. dinoflagellates and ciliates) were shown to prey on the large population of *Crocosphaera* in the NPSG (Dugenne et al. 2020). These small grazers generally dominate zooplankton biomass most of the year (Pasulka et al. 2013), as expected given their fast growth rates (Sherr and Sherr 1994) and the wide size spectrum of prey they can ingest (Hansen et al. 1994).

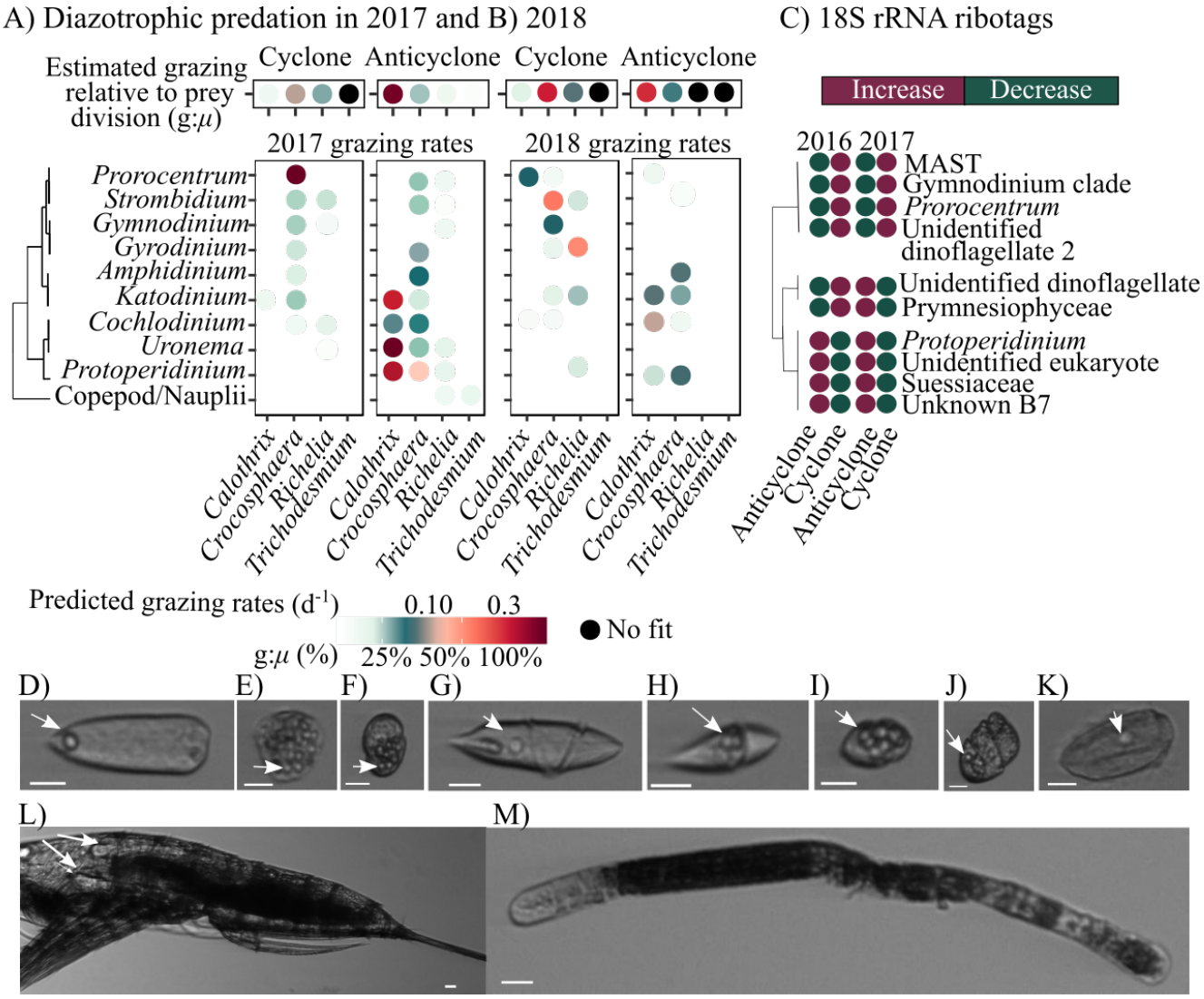

Figure 7: Hierarchical clustering of surface protist populations (top ten) based on predator-prey modeling (A-B) and 18S rRNA ribotags (C) collected during the eddy cruises. Grazing rates (bottom panel) and C demand (top panel) of putative diazotrophic predators were estimated for the 2017 (A) and 2018 (B) cruises. Note that grazing rates of copepods and nauplii have a high uncertainty, since their abundances were not accurately measured by the IFCb. The proxy for C demand, g:μ, represents the ratio of the overall grazing rates on diazotrophs (g) over the average diazotroph intrinsic growth rate, μ(FDC), measured via cell division. The relative abundances of ribotags (C) for some predators (e.g. *Gymnodinium*, *Prorocentrum*, *Protoperidinium*) were systematically enriched in cyclones (top cluster) or anticyclones (bottom cluster) in 2016 and 2017. Purple points indicate a relative increase and green points a relative decrease of ribotags between eddies of the same cruise. Their relative abundance was consistent with a change in estimated grazing rates, confirmed by the IFCb images (D-L): *Prorocentrum* (D), *Strombidium* (E), *Gymnodinium* (E), *Gyrodinium* (G), *Amphidinium* (H), *Katodinium* (K), *Cochlodinium* (J), *Uronema* (K), and Copepod (L), with diazotrophic prey indicated by arrows. Numerous *Trichodesmium* filaments showed signs of cell shrinkage or loss of thylakoids (M), putative markers of programmed cell death or viral lysis. Mixotrophic protists: *Prorocentrum, Strombidium, Gymnodinium*. Heterotrophic protists: *Gyrodinium, Amphidinium, Katodinium, Cochlodinium, Uronema, Protoperidinium*, copepods/nauplii. Scale bars: 10 μm.

By analyzing plankton co-occurrences with a predator-prey model and looking for visual evidence of diazotroph ingestion (Fig. 7D-L), we found that the dinoflagellates *Protoperidinium, Katodinium,* and *Prorocentrum*, the ciliates *Strombidium* and *Uronema,* large copepods, and copepod nauplii are all common predators of diazotrophs in mesoscale eddies of the NPSG (Fig. 7). Predictions of grazing rates positively correlated with independent estimates of grazer in situ growth rates (measured by the fraction of dividing cells, Fig. S7 and Table S4), suggesting that the consumption of diazotrophs sustains a significant fraction of grazer C demand. The grazing pressure, represented by the ratio of the overall grazing rate of a

diazotroph to its average intrinsic growth rate (g:μ), was highest for *Crocosphaera* and *Calothrix*, which were estimated to sustain on average 64 ± 32 and 107 ± 130% of total grazer C demands, respectively (Fig. 7A-B top row). Taxa-specific grazing rates were generally highest for heterotrophic dinoflagellates (0.29 ± 0.24 d^{-1}), followed by mixotrophic ciliates and dinoflagellates (0.18 ± 0.19 d^{-1} and 0.16 ± 0.18 d^{-1} respectively, Fig. 7A-B), consistent with trends from the RNA:DNA proxy for grazer activity observed by Hu et al. (2018) in the NPSG.

Predicted losses due to grazing were always below 0.1 d^{-1} for large/endosymbiotic diazotrophs (i.e. *Trichodesmium* and *Richelia*), while they exceeded 0.3 d^{-1} for smaller free-living or epiphytic cells (i.e. *Crocosphaera* and *Calothrix*). Diazotroph life traits (e.g. size, ecto/endosymbiosis) are important factors influencing prey selectivity. As reviewed in Kirchman (2012), protistan grazing is primarily size-selective, but laboratory studies have suggested that grazing on diazotrophs also depends on the timing of N_2 fixation as a consequence of diel changes in C:N stoichiometry altering the nutritional quality of prey (Deng et al. 2020). Since *Crocosphaera* and the vegetative cells of *Calothrix* have relatively small sizes, low C:N ratios (Table 2), and can be found at high concentrations during the summer (Fig. 3), it is not surprising that they both constitute prime targets for grazers.

2.3.2 Eddy-driven diazotrophic grazing

Grazer C demand met by the ingestion of large *Crocosphaera* and *Calothrix* varied with eddy polarity, inducing significant changes in the proportion of new cells directly lost by grazing, g:μ (Table S3). Predicted g:μ were consistently higher in cyclones for *Crocosphaera* and in anticyclones for *Calothrix* (Fig. 7A-B). The high C demand for *Calothrix* in 2017 and 2018 may explain why the *nifH* gene abundances of Het-3 were close to or below detection limits in anticyclones. Likewise, the low grazer C demand for *Crocosphaera* in anticyclones (Fig. 7A-B) may help explain why *Crocosphaera* abundances were much higher in the anticyclone in 2017, leading to a net accumulation of C production, and ultimately to higher bulk NFRs (Fig. 3).

The difference in grazing pressure between eddies appears linked to the abundance and activity of specific grazer taxa, as revealed by the clustering analysis of protist grazing rates (Fig. 7A-B) and by the relative abundances of grazer 18S rRNA ribotags (Fig. 7C). While a few taxa had higher grazing rates in cyclones, including *Gymnodinium* (0.06 ± 0.03 d^{-1} in the cyclone and not detected in the anticyclone) and *Prorocentrum* (0.43 ± 0.17 d^{-1} in the cyclone and not detected in the anticyclone), most groups grazed upon diazotrophs at higher rates in anticyclones. Additionally, ribotag clustering revealed that the signals of some predators were repeatedly enriched in anticyclones or in cyclones; for instance, the relative abundance of the ribotag for the putative diazotrophic grazer *Protoperidinium* was consistently higher in anticyclones (Fig. 7C). It is unclear what factors drove the differences in protist communities between eddies, but it appears that most mixotrophic taxa (e.g. *Prorocentrum*, *Gymnodinium,* and *Strombidium*) were dominant in cyclones, while numerous heterotrophic taxa (e.g. *Protoperidinium*, nauplii, and *Uronema*) were more active and abundant in anticyclones. We hypothesize that specific trophic strategies (i.e. mixotrophy and heterotrophy) may be linked to the mechanisms driving these patterns between eddies.

Conclusions

This study examined NFRs, cyanobacterial diazotroph abundances, and the mechanisms affecting N_2 fixation within mesoscale eddies of the NPSG. Our observations, in agreement with several previous studies, suggest that anticyclonic eddies sometimes promote anomalously high NFRs. However, the relationship between eddy polarity and NFRs was inverted on one eddy cruise, supporting the low correlation between SLA and NFRs in the NPSG. Likewise, there were inconsistencies among eddy polarity, diazotroph abundances, and several abiotic factors affecting cell-specific activity (light, temperature, and dFe concentrations).

Since high NFRs can result from elevated diazotroph biomass and/or cell-specific activity, we used fine-scale sampling strategies to examine mechanisms that can increase biomass or growth rates within mesoscale eddies. We found robust evidence supporting three mechanisms by which mesoscale eddies

affect diazotrophy: bottom-up control (eddy-driven PO_4^{3-} concentrations), top-down interactions (eddy-driven grazer communities), and the physical accumulation of cells (eddy-driven downwelling).

Our results underscore the importance of the small diazotrophs *Crocosphaera* and UCYN-A to bulk NFRs in the NPSG. By tracking cell division and predicting grazing rates for the former, we observed that anticyclonic eddies may have favored both the growth and the net accumulation of *Crocosphaera*. High growth rates appear driven by positive PO_4^{3-} anomalies, as observations of dividing cells, incubations, and P-stress marker gene expression all predicted the alleviation of *Crocosphaera* P-limitation in the 2017 anticyclone. The net accumulation of cells in the anticyclone was also partially enabled by reduced grazing pressure from different protistan communities.

We found evidence that *Trichodesmium* and *Richelia* were physically accumulated at the cyclonic side of the eddy-eddy front in 2017. Abundances of these large diazotrophs were low in eddy centers where NFRs were measured; thus, physical accumulation did not appear to be a dominant mechanism driving our observations of anomalously high NFRs in anticyclones. Nevertheless, the evidence for physical accumulation presented here agrees with previous reports of elevated *Trichodesmium* and DDA abundances associated with mesoscale eddies. This mechanism likely promotes elevated NFRs near downwelling fronts.

Our Lagrangian sampling approach within eddy centers demonstrated relatively low variability in the cell abundances of small diazotrophs but large fluctuations in *Trichodesmium* and DDA abundances, suggesting that the contributions of these large diazotrophs to NFRs can be variable within an eddy. Such variability highlights the need to resolve fine-scale NFRs and account for the patchiness of plankton communities (including diazotrophs and their predators). Future efforts should also investigate the role of additional resources, such as DOP and silicate (for DDAs), and should explore the factors controlling NFRs by UCYN-A and non-cyanobacterial diazotrophs. Together, our observations and analyses help to elucidate the complex ways through which mesoscale eddies of both polarities may promote N_2 fixation in the oceans.

Acknowledgements

This work was funded by the Simons Foundation (Award # 329104 to EVA, MJC, EFD, STD, SJ, DMK, AEW, and JPZ). We are thankful to the chief scientists, including Tara Clemente (2017) and Steve Poulos (2018), as well as the captains and crew members of the eddy cruises. We are also grateful to Eric Shimabukuro, Ryan Tabata, and Tim Burrell for their help with field operations, as well as Katie Watkins-Brandt for valuable support with the IFCb and microscopic analysis for the 2017 expedition.

References

Aldeco-Ramírez, J., M. Monreal-Gómez, M. Signoret, D. Salas-de-León, and D. Hernández-Becerril. 2009. Occurrence of a subsurface anticyclonic eddy, fronts, and *Trichodesmium* spp. Cienc. Mar. **35:** 333-344.

Azimuddin, K. M. and others 2016. Possible association of diazotrophs with marine zooplankton in the Pacific Ocean. Microbiologyopen **5:** 1016-1026.

Bach, L. T., U. Riebesell, S. Sett, S. Febiri, P. Rzepka, and K. G. Schulz. 2012. An approach for particle sinking velocity measurements in the 3–400 µm size range and considerations on the effect of temperature on sinking rates. Mar. Biol. **159:** 1853-1864.

Barone, B., A. R. Coenen, S. J. Beckett, D. J. McGillicuddy, J. S. Weitz, and D. M. Karl. 2019. The ecological and biogeochemical state of the North Pacific Subtropical Gyre is linked to sea surface height. J. Mar. Res. **77:** 215-245.

Basu, S., M. Gledhill, D. de Beer, S. P. Matondkar, and Y. Shaked. 2019. Colonies of marine cyanobacteria *Trichodesmium* interact with associated bacteria to acquire iron from dust. Commun. Biol. **2:** 1-8.

Benavides, M., N. S. Agawin, J. Arístegui, P. Ferriol, and L. J. Stal. 2011. Nitrogen fixation by *Trichodesmium* and small diazotrophs in the subtropical northeast Atlantic. Aquat. Microb. Ecol. **65:** 43-53.

Benavides, M. and others 2020. Dissolved organic matter stimulates N_2 fixation and *nifH* gene expression in *Trichodesmium*. FEMS Microbiol. Lett. **367:** fnaa034.

Benitez-Nelson, C. R. and others 2007. Mesoscale eddies drive increased silica export in the subtropical Pacific Ocean. Science **316:** 1017-1021.

Berman-Frank, I., K. D. Bidle, L. Haramaty, and P. G. Falkowski. 2004. The demise of the marine cyanobacterium, *Trichodesmium* spp., via an autocatalyzed cell death pathway. Limnol. Oceanogr. **49:** 997-1005.

1114 Berman-Frank, I., J. T. Cullen, Y. Shaked, R. M. Sherrell, and P. G. Falkowski. 2001. Iron availability,
1115 cellular iron quotas, and nitrogen fixation in *Trichodesmium*. Limnol Oceanogr **46:** 1249-1260.
1116 Berman-Frank, I., A. Quigg, Z. V. Finkel, A. J. Irwin, and L. Haramaty. 2007. Nitrogen-fixation strategies
1117 and Fe requirements in cyanobacteria. Limnol. Oceanogr. **52:** 2260-2269.
1118 Björkman, K. M., S. Duhamel, and D. M. Karl. 2012. Microbial group specific uptake kinetics of inorganic
1119 phosphate and adenosine-5′-triphosphate (ATP) in the North Pacific Subtropical Gyre. Front.
1120 Microbiol. **3:** 189.
1121 Boatman, T. G., T. Lawson, and R. J. Geider. 2017. A key marine diazotroph in a changing ocean: The
1122 interacting effects of temperature, CO_2 and light on the growth of *Trichodesmium erythraeum*
1123 IMS101. PLoS One **12:** e0168796.
1124 Boatman, T. G., K. Oxborough, M. Gledhill, T. Lawson, and R. J. Geider. 2018. An integrated response of
1125 *Trichodesmium erythraeum* IMS101 growth and photo-physiology to iron, CO_2, and light intensity.
1126 Front. Microbiol. **9:** 624.
1127 Bolger, A. M., M. Lohse, and B. Usadel. 2014. Trimmomatic: a flexible trimmer for Illumina sequence
1128 data. Bioinformatics **30:** 2114-2120.
1129 Bonett, D. G., and T. A. Wright. 2000. Sample size requirements for estimating Pearson, Kendall and
1130 Spearman correlations. Psychometrika **65:** 23-28.
1131 Böttjer, D. and others 2017. Temporal variability of nitrogen fixation and particulate nitrogen export at
1132 Station ALOHA. Limnol. Oceanogr. **62:** 200-216.
1133 Böttjer, D., D. M. Karl, R. M. Letelier, D. A. Viviani, and M. J. Church. 2014. Experimental assessment of
1134 diazotroph responses to elevated seawater pCO_2 in the North Pacific Subtropical Gyre. Global
1135 Biogeochem. Cycles **28:** 601-616.
1136 Brauer, V. S. and others 2013. Low temperature delays timing and enhances the cost of nitrogen fixation in
1137 the unicellular cyanobacterium *Cyanothece*. ISME J. **7:** 2105-2115.

1138 Breitbarth, E., A. Oschlies, and J. LaRoche. 2007. Physiological constraints on the global distribution of
1139 *Trichodesmium*? Effect of temperature on diazotrophy. Biogeosciences **4:** 53-61.
1140 Bushmanova, E., D. Antipov, A. Lapidus, and A. D. Prjibelski. 2019. rnaSPAdes: a de novo transcriptome
1141 assembler and its application to RNA-Seq data. GigaScience **8:** giz100.
1142 Cheung, S. and others 2020. Physical forcing controls the basin-scale occurrence of nitrogen-fixing
1143 organisms in the North Pacific Ocean. Global Biogeochem. Cy.**:** e2019GB006452.
1144 Church, M. J., K. M. Björkman, D. M. Karl, M. A. Saito, and J. P. Zehr. 2008. Regional distributions of
1145 nitrogen-fixing bacteria in the Pacific Ocean. Limnol. Oceanogr. **53:** 63-77.
1146 Church, M. J., B. D. Jenkins, D. M. Karl, and J. P. Zehr. 2005a. Vertical distributions of nitrogen-fixing
1147 phylotypes at Stn ALOHA in the oligotrophic North Pacific Ocean. Aquat. Microb. Ecol. **38:** 3-14.
1148 Church, M. J., C. Mahaffey, R. M. Letelier, R. Lukas, J. P. Zehr, and D. M. Karl. 2009. Physical forcing of
1149 nitrogen fixation and diazotroph community structure in the North Pacific subtropical gyre. Global
1150 Biogeochem. Cy. **23:** GB2020.
1151 Church, M. J., C. M. Short, B. D. Jenkins, D. M. Karl, and J. P. Zehr. 2005b. Temporal patterns of
1152 nitrogenase gene (*nifH*) expression in the oligotrophic North Pacific Ocean. Appl. Environ.
1153 Microbiol. **71:** 5362-5370.
1154 Conroy, B. J., D. K. Steinberg, B. Song, A. Kalmbach, E. J. Carpenter, and R. A. Foster. 2017.
1155 Mesozooplankton graze on cyanobacteria in the Amazon River plume and western tropical North
1156 Atlantic. Front. Microbiol. **8:** 1436.
1157 Cornejo-Castillo, F. M. and others 2019. UCYN-A3, a newly characterized open ocean sublineage of the
1158 symbiotic N_2-fixing cyanobacterium *Candidatus* Atelocyanobacterium thalassa. Environ.
1159 Microbiol. **21:** 111-124.
1160 D'Asaro, E. A. and others 2018. Ocean convergence and the dispersion of flotsam. Proc. Natl. Acad. Sci.
1161 U.S.A. **115:** 1162-1167.

Davis, C. S., and D. J. McGillicuddy. 2006. Transatlantic abundance of the N_2-fixing colonial cyanobacterium *Trichodesmium*. Science **312:** 1517-1520.

Deng, L., S. Cheung, and H. Liu. 2020. Protistal grazers increase grazing on unicellular cyanobacteria diazotroph at night. Front. Mar. Sci.

Dufois, F., N. J. Hardman-Mountford, J. Greenwood, A. J. Richardson, M. Feng, and R. J. Matear. 2016. Anticyclonic eddies are more productive than cyclonic eddies in subtropical gyres because of winter mixing. Science Advances **2:** e1600282.

Dugenne, M., F. Henderikx Freitas, S. T. Wilson, D. M. Karl, and A. E. White. 2020. Life and death of *Crocosphaera* sp. in the Pacific Ocean: Fine scale predator–prey dynamics. Limnol. Oceanogr. **65:** 2603-2617.

Dyhrman, S. and others 2006. Phosphonate utilization by the globally important marine diazotroph *Trichodesmium*. Nature **439:** 68-71.

Dyhrman, S. T., and S. T. Haley. 2006. Phosphorus scavenging in the unicellular marine diazotroph *Crocosphaera watsonii*. Appl. Environ. Microbiol. **72:** 1452-1458.

Ferrón, S., D. A. del Valle, K. M. Björkman, P. D. Quay, M. J. Church, and D. M. Karl. 2016. Application of membrane inlet mass spectrometry to measure aquatic gross primary production by the ^{18}O *in vitro* method. Limnol. Oceanogr.-Meth. **14:** 610-622.

Finkel, Z., A. Quigg, J. Raven, J. Reinfelder, O. Schofield, and P. Falkowski. 2006. Irradiance and the elemental stoichiometry of marine phytoplankton. Limnol. Oceanogr. **51:** 2690-2701.

Fitzsimmons, J. N. and others 2015. Daily to decadal variability of size-fractionated iron and iron-binding ligands at the Hawaii Ocean Time-series Station ALOHA. Geochim. Cosmochim. Acta **171:** 303-324.

Follett, C. L., S. Dutkiewicz, D. M. Karl, K. Inomura, and M. J. Follows. 2018a. Seasonal resource conditions favor a summertime increase in North Pacific diatom–diazotroph associations. ISME J. **12:** 1543-1557.

1187 Follett, C. L., A. E. White, S. T. Wilson, and M. J. Follows. 2018b. Nitrogen fixation rates diagnosed from
1188 diurnal changes in elemental stoichiometry. Limnol. Oceanogr. **63:** 1911-1923.
1189 Fong, A. A., D. M. Karl, R. Lukas, R. M. Letelier, J. P. Zehr, and M. J. Church. 2008. Nitrogen fixation in
1190 an anticyclonic eddy in the oligotrophic North Pacific Ocean. ISME J. **2:** 663–676.
1191 Foreman, R. K., M. Segura-Noguera, and D. M. Karl. 2016. Validation of Ti (III) as a reducing agent in the
1192 chemiluminescent determination of nitrate and nitrite in seawater. Mar. Chem. **186:** 83-89.
1193 Foster, R., A. Subramaniam, C. Mahaffey, E. Carpenter, D. Capone, and J. Zehr. 2007. Influence of the
1194 Amazon River plume on distributions of free-living and symbiotic cyanobacteria in the western
1195 tropical north Atlantic Ocean. Limnol. Oceanogr. **52:** 517-532.
1196 Foster, R. A., N. L. Goebel, and J. P. Zehr. 2010. Isolation of *Calothrix rhizosoleniae* (cyanobacteria)
1197 strain SC01 from *Chaetoceros* (Bacillariophyta) spp. diatoms of the subropical North Pacific
1198 Ocean. J. Phycol. **46:** 1028-1037.
1199 Foster, R. A., M. M. Kuypers, T. Vagner, R. W. Paerl, N. Musat, and J. P. Zehr. 2011. Nitrogen fixation
1200 and transfer in open ocean diatom–cyanobacterial symbioses. ISME J. **5:** 1484-1493.
1201 Fu, F.-X. and others 2014. Differing responses of marine N_2 fixers to warming and consequences for future
1202 diazotroph community structure. Aquat. Microb. Ecol. **72:** 33-46.
1203 Fu, L., B. Niu, Z. Zhu, S. Wu, and W. Li. 2012. CD-HIT: accelerated for clustering the next-generation
1204 sequencing data. Bioinformatics **28:** 3150-3152.
1205 Garcia, N. and others 2013a. Combined effects of CO_2 and light on large and small isolates of the
1206 unicellular N_2-fixing cyanobacterium *Crocosphaera watsonii* from the western tropical Atlantic
1207 Ocean. Eur. J. Phycol. **48:** 128-139.
1208 Garcia, N. S., F. Fu, P. N. Sedwick, and D. A. Hutchins. 2015. Iron deficiency increases growth and
1209 nitrogen-fixation rates of phosphorus-deficient marine cyanobacteria. ISME J. **9:** 238-245.

Garcia, N. S., F.-X. Fu, and D. A. Hutchins. 2013b. Colimitation of the unicellular photosynthetic diazotroph *Crocosphaera watsonii* by phosphorus, light, and carbon dioxide. Limnol. Oceanogr. **58:** 1501-1512.

Gaube, P., D. B. Chelton, R. M. Samelson, M. G. Schlax, and L. W. O'Neill. 2015. Satellite observations of mesoscale eddy-induced Ekman pumping. J. Phys. Oceanogr. **45:** 104-132.

Gaube, P., D. J. McGillicuddy Jr, and A. J. Moulin. 2019. Mesoscale eddies modulate mixed layer depth globally. Geophys. Res. Lett. **46:** 1505-1512.

Goebel, N. L., C. A. Edwards, B. J. Carter, K. M. Achilles, and J. P. Zehr. 2008. Growth and carbon content of three different-sized diazotrophic cyanobacteria observed in the Subtropical North Pacific. J. Phycol. **44:** 1212-1220.

Goebel, N. L., C. A. Edwards, M. J. Church, and J. P. Zehr. 2007. Modeled contributions of three types of diazotrophs to nitrogen fixation at Station ALOHA. ISME J. **1:** 606-619.

Gradoville, M. R., B. C. Crump, M. J. Church, R. M. Letelier, and A. E. White. 2017. Microbiome of *Trichodesmium* colonies from the North Pacific Subtropical Gyre. Front. Microbiol. **8:** 1122.

Gradoville, M. R. and others 2020. Latitudinal constraints on the abundance and activity of the cyanobacterium UCYN-A and other marine diazotrophs in the North Pacific. Limnol. Oceanogr. **65:** 1858-1875.

Guidi, L. and others 2012. Does eddy-eddy interaction control surface phytoplankton distribution and carbon export in the North Pacific Subtropical Gyre? J. Geophys. Res. Biogeosci. **117:** G02024.

Guo, M., P. Xiu, F. Chai, and H. Xue. 2019. Mesoscale and submesoscale contributions to high sea surface chlorophyll in subtropical gyres. Geophys. Res. Lett. **46:** 13217-13226.

Hansen, B., P. K. Bjornsen, and P. J. Hansen. 1994. The size ratio between planktonic predators and their prey. Limnol. Oceanogr. **39:** 395-403.

Harke, M. J., K. R. Frischkorn, S. T. Haley, F. O. Aylward, J. P. Zehr, and S. T. Dyhrman. 2019. Periodic and coordinated gene expression between a diazotroph and its diatom host. ISME J. **13:** 118-131.

Hawco, N. J. and others 2020a. Minimal cobalt metabolism in the marine cyanobacterium *Prochlorococcus*. Proc. Natl. Acad. Sci. U.S.A. **117:** 15740-15747.

Hawco, N. J. and others 2020b. Metal isotope signatures from lava-seawater interaction during the 2018 eruption of Kīlauea. Geochim. Cosmochim. Acta **282:** 340-356.

Hewson, I., S. R. Govil, D. G. Capone, E. J. Carpenter, and J. A. Fuhrman. 2004. Evidence of *Trichodesmium* viral lysis and potential significance for biogeochemical cycling in the oligotrophic ocean. Aquat. Microb. Ecol. **36:** 1-8.

Holl, C. M., A. M. Waite, S. Pesant, P. A. Thompson, and J. P. Montoya. 2007. Unicellular diazotrophy as a source of nitrogen to Leeuwin Current coastal eddies. Deep Sea Res. Part II Top. Stud. Oceanogr. **54:** 1045-1054.

Hoppe, K. S. 2013. The sinking rate and transparent exopolymer particle (TEP) production of *Hemiaulus hauckii.* Doctoral dissertation. University of Texas at Austin.

Hu, S. K., P. E. Connell, L. Y. Mesrop, and D. A. Caron. 2018. A hard day's night: Diel shifts in microbial eukaryotic activity in the North Pacific Subtropical Gyre. Front. Mar. Sci. **5:** 351.

Hunt, B. P., S. Bonnet, H. Berthelot, B. J. Conroy, R. A. Foster, and M. Pagano. 2016. Contribution and pathways of diazotroph-derived nitrogen to zooplankton during the VAHINE mesocosm experiment in the oligotrophic New Caledonia lagoon. Biogeosciences **13:** 3131.

Hyatt, D., G.-L. Chen, P. F. LoCascio, M. L. Land, F. W. Larimer, and L. J. Hauser. 2010. Prodigal: prokaryotic gene recognition and translation initiation site identification. BMC Bioinformatics **11:** 1-11.

Jacq, V., C. Ridame, S. l'Helguen, F. Kaczmar, and A. Saliot. 2014. Response of the unicellular diazotrophic cyanobacterium *Crocosphaera watsonii* to iron limitation. PLoS One **9:** e86749.

Jassby, A. D., and T. Platt. 1976. Mathematical formulation of the relationship between photosynthesis and light for phytoplankton. Limnol. Oceanogr. **21:** 540-547.

Karl, D. and others 1996. Seasonal and interannual variability in primary production and particle flux at Station ALOHA. Deep Sea Res. Part II Top. Stud. Oceanogr. **43:** 539-568.

Karl, D., R. Letelier, L. Tupas, J. Dore, J. Christian, and D. Hebel. 1997. The role of nitrogen fixation in biogeochemical cycling in the subtropical North Pacific Ocean. Nature **388:** 533-538.

Karl, D. and others 2002. Dinitrogen fixation in the world's oceans. Biogeochemistry **57:** 47-98.

Karl, D. M. and others 2001. Ecological nitrogen-to-phosphorus stoichiometry at station ALOHA. Deep Sea Res. Part II Top. Stud. Oceanogr. **48:** 1529-1566.

Karl, D. M., and M. J. Church. 2014. Microbial oceanography and the Hawaii Ocean Time-series programme. Nat. Rev. Microbiol. **12:** 699-713.

---. 2017. Ecosystem structure and dynamics in the North Pacific Subtropical Gyre: new views of an old ocean. Ecosystems **20:** 433-457.

Karl, D. M., M. J. Church, J. E. Dore, R. M. Letelier, and C. Mahaffey. 2012. Predictable and efficient carbon sequestration in the North Pacific Ocean supported by symbiotic nitrogen fixation. Proc. Natl. Acad. Sci. U.S.A. **109:** 1842-1849.

Karl, D. M., and G. Tien. 1992. MAGIC: A sensitive and precise method for measuring dissolved phosphorus in aquatic environments. Limnol. Oceanogr. **37:** 105-116.

Kirchman, D. L. 2012. Predation and protists. Processes in Microbial Ecology. Oxford University Press.

Knapp, A. N. 2012. The sensitivity of marine N_2 fixation to dissolved inorganic nitrogen. Front. Microbiol. **3:** 374.

Knapp, A. N., J. Dekaezemacker, S. Bonnet, J. A. Sohm, and D. G. Capone. 2012. Sensitivity of *Trichodesmium erythraeum* and *Crocosphaera watsonii* abundance and N_2 fixation rates to varying NO_3^- and PO_4^{3-} concentrations in batch cultures. Aquat. Microb. Ecol. **66:** 223-236.

Krupke, A. and others 2013. *In situ* identification and N_2 and C fixation rates of uncultivated cyanobacteria populations. Syst. Appl. Microbiol. **36:** 259–271.

Landolfi, A., W. Koeve, H. Dietze, P. Kähler, and A. Oschlies. 2015. A new perspective on environmental controls of marine nitrogen fixation. Geophys. Res. Lett. **42:** 4482-4489.

Landry, M. R. and others 2008. Depth-stratified phytoplankton dynamics in Cyclone Opal, a subtropical mesoscale eddy. Deep Sea Res. Part II Top. Stud. Oceanogr. **55:** 1348-1359.

Letelier, R. M. and others 2019. Climate-driven oscillation of phosphorus and iron limitation in the North Pacific Subtropical Gyre. Proc. Natl. Acad. Sci. U.S.A. **116:** 12720-12728.

Letelier, R. M., A. E. White, R. R. Bidigare, B. Barone, M. J. Church, and D. M. Karl. 2017. Light absorption by phytoplankton in the North Pacific Subtropical Gyre. Limnol. Oceanogr. **62:** 1526-1540.

Li, H. 2015. BFC: correcting Illumina sequencing errors. Bioinformatics **31:** 2885-2887.

Liu, J. and others 2020. Effect of mesoscale eddies on diazotroph community structure and nitrogen fixation rates in the South China Sea. Reg. Stud. Mar. Sci. **35:** 101106.

Löscher, C. and others 2016. N_2 fixation in eddies of the eastern tropical South Pacific Ocean. Biogeosciences **13:** 2889-2899.

Luo, E., J. M. Eppley, A. E. Romano, D. R. Mende, and E. F. DeLong. 2020. Double-stranded DNA virioplankton dynamics and reproductive strategies in the oligotrophic open ocean water column. ISME J **14:** 1304-1315.

Luo, Y.-W., I. Lima, D. Karl, C. Deutsch, and S. Doney. 2014. Data-based assessment of environmental controls on global marine nitrogen fixation. Biogeosciences **11:** 691-708.

Mahadevan, A. 2016. The impact of submesoscale physics on primary productivity of plankton. Ann. Rev. Mar. Sci. **8:** 161-184.

McDuff, R., and S. Chisholm. 1982. The calculation of in situ growth rates of phytoplankton populations from fractions of cells undergoing mitosis: A clarification. Limnol Oceanogr **27:** 783-788.

McGillicuddy, D., and P. J. Franks. 2019. Models of plankton patchiness. Encyclopedia of Ocean Sciences **5:** 536-546.

McGillicuddy, D., and A. Robinson. 1997. Eddy-induced nutrient supply and new production in the Sargasso Sea. Deep Sea Res. Part I Oceanogr. Res. Pap. **44:** 1427-1450.

McGillicuddy, D. and others 1998. Influence of mesoscale eddies on new production in the Sargasso Sea. Nature **394:** 263-266.

McGillicuddy, D. J. 2016. Mechanisms of physical-biological-biogeochemical interaction at the oceanic mesoscale. Ann. Rev. Mar. Sci. **8:** 125-159.

Menden-Deuer, S., and E. J. Lessard. 2000. Carbon to volume relationships for dinoflagellates, diatoms, and other protist plankton. Limnol. Oceanogr. **45:** 569-579.

Meyer, N. R., J. Fortney, and A. E. Dekas. 2020. NanoSIMS sample preparation decreases isotope enrichment: magnitude, variability and implications for single-cell rates of microbial activity. Environ. Microbiol.**:** doi: 10.1111/1462-2920.15264.

Mohr, W., T. Großkopf, D. W. R. Wallace, and J. LaRoche. 2010. Methodological underestimation of oceanic nitrogen fixation rates. PLoS One **5:** e12583.

Moisander, P. H. and others 2010. Unicellular cyanobacterial distributions broaden the oceanic N_2 fixation domain. Science **327:** 1512-1514.

Moisander, P. H., R. A. Beinart, M. Voss, and J. P. Zehr. 2008. Diversity and abundance of diazotrophic microorganisms in the South China Sea during intermonsoon. ISME J. **2:** 954-967.

Moisander, P. H., M. Benavides, S. Bonnet, I. Berman-Frank, A. E. White, and L. Riemann. 2017. Chasing after non-cyanobacterial nitrogen fixation in marine pelagic environments. Front. Microbiol. **8:** 1736.

Montoya, J. P., M. Voss, P. Kahler, and D. G. Capone. 1996. A simple, high-precision, high-sensitivity tracer assay for N_2 fixation. Appl. Environ. Microbiol. **62:** 986-993.

Mulholland, M. 2007. The fate of nitrogen fixed by diazotrophs in the ocean. Biogeosciences **4:** 37-51.

O'Neil, J., P. Metzler, and P. Glibert. 1996. Ingestion of $^{15}N_2$-labelled *Trichodesmium* spp. and ammonium regeneration by the harpacticoid copepod *Macrosetella gracilis*. Mar. Biol. **125:** 89-96.

O'Neil, J. M. 1998. The colonial cyanobacterium *Trichodesmium* as a physical and nutritional substrate for the harpacticoid copepod *Macrosetella gracilis*. J. Plankton Res. **20:** 43-59.

Olson, E. M., D. J. McGillicuddy, G. R. Flierl, C. S. Davis, S. T. Dyhrman, and J. B. Waterbury. 2015. Mesoscale eddies and *Trichodesmium* spp. distributions in the southwestern North Atlantic. J. Geophys. Res. Oceans **120:** 4129-4150.

Parks, D. H. and others 2018. A standardized bacterial taxonomy based on genome phylogeny substantially revises the tree of life. Nat. Biotechnol. **36:** 996-1004.

Pasulka, A. L., M. R. Landry, D. A. Taniguchi, A. G. Taylor, and M. J. Church. 2013. Temporal dynamics of phytoplankton and heterotrophic protists at station ALOHA. Deep Sea Res. Part II Top. Stud. Oceanogr. **93:** 44-57.

Pereira, N., I. N. Shilova, and J. P. Zehr. 2016. Molecular markers define progressing stages of phosphorus limitation in the nitrogen-fixing cyanobacterium, *Crocosphaera*. J. Phycology **52:** 274-282.

Pilo, G. S., P. R. Oke, R. Coleman, T. Rykova, and K. Ridgway. 2018. Patterns of vertical velocity induced by eddy distortion in an ocean model. J. Geophys. Res. Oceans **123:** 2274-2292.

Pinedo-González, P. and others 2020. Anthropogenic Asian aerosols provide Fe to the North Pacific Ocean. Proc. Natl. Acad. Sci. U.S.A. **117:** 27862-27868.

Poff, K. E., A. O. Leu, J. M. Eppley, D. M. Karl, and E. F. DeLong. 2021. Microbial dynamics of elevated carbon flux in the open ocean's abyss. Proc. Natl. Acad. Sci. U.S.A. **118:** e2018269118.

Quast, C. and others 2013. The SILVA ribosomal RNA gene database project: improved data processing and web-based tools. Nucleic Acids Res. **41:** D590-D596.

Rahav, E., B. Herut, N. Stambler, E. Bar-Zeev, M. R. Mulholland, and I. Berman-Frank. 2013. Uncoupling between dinitrogen fixation and primary productivity in the eastern Mediterranean Sea. J .Geophys. Res. Biogeosciences **118:** 195-202.

Ribalet, F. and others 2019. SeaFlow data v1, high-resolution abundance, size and biomass of small phytoplankton in the North Pacific. Sci. Data **6:** 1-8.

Robidart, J. C. and others 2014. Ecogenomic sensor reveals controls on N_2-fixing microorganisms in the North Pacific Ocean. ISME J. **8:** 1175.

Rouco, M., K. R. Frischkorn, S. T. Haley, H. Alexander, and S. T. Dyhrman. 2018. Transcriptional patterns identify resource controls on the diazotroph *Trichodesmium* in the Atlantic and Pacific oceans. ISME J. **12:** 1486-1495.

Sargent, E. C. and others 2016. Evidence for polyploidy in the globally important diazotroph *Trichodesmium*. FEMS Microbiol. Lett. **363:** fnw244.

Scavotto, R. E., C. Dziallas, M. Bentzon-Tilia, L. Riemann, and P. H. Moisander. 2015. Nitrogen-fixing bacteria associated with copepods in coastal waters of the North Atlantic Ocean. Environ. Microbiol. **17:** 3754-3765.

Sherr, E., and B. Sherr. 1994. Bacterivory and herbivory: key roles of phagotrophic protists in pelagic food webs. Microb. Ecol. **28:** 223-235.

Sosik, H. M., and R. J. Olson. 2007. Automated taxonomic classification of phytoplankton sampled with imaging-in-flow cytometry. Limnol. Oceanogr.-Meth. **5:** 204-216.

Stenegren, M. 2020. Significance of N_2 fixing planktonic symbioses for open ocean ecosystems. Department of ecology, environment and plant sciences, Stockholm University.

Stukel, M. R., V. J. Coles, M. Brooks, and R. R. Hood. 2014. Top-down, bottom-up and physical controls on diatom-diazotroph assemblage growth in the Amazon River plume. Biogeosciences **11:** 3259-3278.

Taboada, F. G., R. G. Gil, J. Höfer, S. González, and R. Anadón. 2010. *Trichodesmium* spp. population structure in the eastern North Atlantic subtropical gyre. Deep Sea Res. Part I Oceanogr. Res. Pap. **57:** 65-77.

Taniuchi, Y., Y. l. L. Chen, H. Y. Chen, M. L. Tsai, and K. Ohki. 2012. Isolation and characterization of the unicellular diazotrophic cyanobacterium Group C TW3 from the tropical western Pacific Ocean. Environ. Microbiol. **14:** 641-654.

Thompson, A., B. J. Carter, K. Turk-Kubo, F. Malfatti, F. Azam, and J. P. Zehr. 2014. Genetic diversity of the unicellular nitrogen-fixing cyanobacteria UCYN-A and its prymnesiophyte host. Environ. Microbiol. **16:** 3238-3249.

Tibshirani, R. and others 2012. Strong rules for discarding predictors in lasso-type problems. J. R. Stat. Soc. Series B Stat. Methodol. **74:** 245-266.

Tuit, C., J. Waterbury, and G. Ravizza. 2004. Diel variation of molybdenum and iron in marine diazotrophic cyanobacteria. Limnol Oceanogr **49:** 978-990.

Tuo, S. 2015. The distributions and the mechanisms of the cyanobionts and their host diatoms in the northern South China Sea and the Kuroshio. Doctoral dissertation, National Sun Yat-sen University.

Tuo, S.-H., Y.-L. Lee Chen, H.-Y. Chen, and T.-Y. Chen. 2017. Free-living heterocystous cyanobacteria in the tropical marginal seas of the western North Pacific. J. Plankton Res. **39:** 404-422.

Turk-Kubo, K. A., P. Connell, D. Caron, M. E. Hogan, H. M. Farnelid, and J. P. Zehr. 2018. *In situ* diazotroph population dynamics under different resource ratios in the North Pacific Subtropical Gyre. Front. Microbiol. **9:** 1616.

Turk-Kubo, K. A., H. M. Farnelid, I. N. Shilova, B. Henke, and J. P. Zehr. 2017. Distinct ecological niches of marine symbiotic N_2-fixing cyanobacterium *Candidatus Atelocyanobacterium thalassa* sublineages. J Phycol **53:** 451-461.

Verity, P. G., C. Y. Robertson, C. R. Tronzo, M. G. Andrews, J. R. Nelson, and M. E. Sieracki. 1992. Relationships between cell volume and the carbon and nitrogen content of marine photosynthetic nanoplankton. Limnol. Oceanogr. **37:** 1434-1446.

Villareal, T., and E. Carpenter. 2003. Buoyancy regulation and the potential for vertical migration in the oceanic cyanobacterium *Trichodesmium*. Microb. Ecol. **45:** 1-10.

Villareal, T. A. 1990. Laboratory culture and preliminary characterization of the nitrogen-fixing *Rhizosolenia-Richelia* symbiosis. Mar. Ecol. **11:** 117-132.

Villareal, T. A., and E. J. Carpenter. 1989. Nitrogen fixation, suspension characteristics, and chemical composition of *Rhizosolenia* mats in the central North Pacific gyre. Biol. Oceanogr. **6:** 327-345.

Walsby, A. 1978. The properties and buoyancy-providing role of gas vacuoles in *Trichodesmium* Ehrenberg. Brit. Phycol. J. **13:** 103-116.

Wannicke, N., M. Benavides, T. Dalsgaard, J. W. Dippner, J. P. Montoya, and M. Voss. 2018. New perspectives on nitrogen fixation measurements using $^{15}N_2$ gas. Front Mar Sci **5:** 120.

Ward, B. A., S. Dutkiewicz, C. M. Moore, and M. J. Follows. 2013. Iron, phosphorus, and nitrogen supply ratios define the biogeography of nitrogen fixation. Limnol. Oceanogr **58:** 2059-2075.

White, A. E. and others 2020. A critical review of the $^{15}N_2$ tracer method to measure diazotrophic production in pelagic ecosystems. Limnol. Oceanogr.-Meth. **18:** 129-147.

White, A. E., Y. H. Spitz, D. M. Karl, and R. M. Letelier. 2006. Flexible elemental stoichiometry in *Trichodesmium* spp. and its ecological implications. Limnol. Oceanogr. **51:** 1777-1790.

White, A. E., K. S. Watkins-Brandt, and M. J. Church. 2018. Temporal variability of *Trichodesmium* spp. and diatom-diazotroph assemblages in the North Pacific Subtropical Gyre. Front. Mar. Sci. **5:** 27.

Wilson, S. T. and others 2017. Coordinated regulation of growth, activity and transcription in natural populations of the unicellular nitrogen-fixing cyanobacterium *Crocosphaera*. Nat. Microbiol. **2:** 17118.

Wilson, S. T., D. Böttjer, M. J. Church, and D. M. Karl. 2012. Comparative assessment of nitrogen fixation methodologies, conducted in the oligotrophic North Pacific Ocean. Appl. Environ. Microbiol. **78:** 6516-6523.

Wozniak, B., J. Dera, D. Ficek, R. Majchrowski, M. Ostrowska, and S. Kaczmarek. 2003. Modelling light and photosynthesis in the marine environment. Oceanologia **45:** 171-245.

Xie, C., C. L. W. Goi, D. H. Huson, P. F. Little, and R. B. Williams. 2016. RiboTagger: fast and unbiased 16S/18S profiling using whole community shotgun metagenomic or metatranscriptome surveys. BMC Bioinformatics **17:** 277-282.

Yoder, J. A., S. G. Ackleson, R. T. Barber, P. Flament, and W. M. Balch. 1994. A line in the sea. Nature **371:** 689-692.

Zehr, J. P. 2011. Nitrogen fixation by marine cyanobacteria. Trends Microbiol. **19:** 162-173.

Zehr, J. P., and D. G. Capone. 2020. Changing perspectives in marine nitrogen fixation. Science **368:** eaay9514.

Zehr, J. P. and others 2001. Unicellular cyanobacteria fix N_2 in the subtropical North Pacific Ocean. Nature **412:** 635-637.